

A CUT-CELL BASED GHOST FLUID METHOD FOR  
MULTI-COMPONENT COMPRESSIBLE FLOWS

by

Chen Liu

A thesis submitted to the faculty of  
The University of North Carolina at Charlotte  
in partial fulfillment of the requirements  
for the degree of Master of Science in  
Mechanical Engineering

Charlotte

2020

Approved by:

---

Dr. Praveen Ramaprabhu

---

Dr. Harish Cherukuri

---

Dr. Shaozhong Deng

©2020  
Chen Liu  
ALL RIGHTS RESERVED

## ABSTRACT

CHEN LIU. A cut-cell based ghost fluid method for multi-component compressible flows. (Under the direction of DR. PRAVEEN RAMAPRABHU)

Multi-material compressible flows are observed in several applications of practical relevance including combustion, cavitation and shock lithotripsy. To solve such flows numerically with improved efficiency and accuracy, the use of the Ghost Fluid Method (GFM) and its derivatives have been adopted widely. However, certain drawbacks of the ghost fluid approach such as overheating errors, and the appearance of unphysical oscillations of density and pressure are well known and have been documented in the literature. In this work, a cut-cell based GFM approach is proposed to accurately solve for the fluid state at the multi-material interface, while the location of the interface is tracked by a second-order level set scheme. The modified GFM was implemented in IMPACT, a multi-material, shock-physics code. The improvements to the GFM are validated through a wide range of simulations including multi-material flow problems, 1D shock problems, 2D shock-induced bubble collapse in water/air and the 2D Richtmyer-Meshkov instability. In addition, the efficiency of the numerical solver is improved with the implementation of a blocked-structured Adaptive Mesh Refinement (AMR) scheme. We find the AMR implementation enhances computational efficiency, while improving the mass conservation properties of the level set scheme.

## ACKNOWLEDGEMENTS

In the first place, I owe my gratitude to my mentor Dr. Praveen Ramaprabhu, who has provided me with invaluable guidance and support on research, writing and presentation. His help and encouragement have given me tons of confidence when I was questioning myself during the course of the research. I would also like to thank Dr. Harish Cherukuri and Dr. Shaozhong Deng for serving as my committee members and providing helpful feedback on my research.

Thirdly, I would like to thank my lab mate, Dr. Pedram Bigdelou, who is always available to help when I ran into difficulties understanding the code or the algorithm. It is incredible that he can explain some of the most obstruct ideas in such a precise and understandable way. I would also like to thank doctoral candidate Prashant Tarey, who shared me with his numerical codes and explained FLASH to me in a very detailed way.

The PARAMESH software used in this work was developed at the NASA Goddard Space Flight Center and Drexel University under NASA's HPCC and ESTO/CT projects and under grant NNG04GP79G from the NASA/AISR project.

## TABLE OF CONTENTS

LIST OF TABLES .....	vii
LIST OF FIGURES .....	viii
CHAPTER 1: INTRODUCTION .....	1
1.1 Objective .....	1
1.2 The Ghost Fluid Method .....	2
1.3 The Level Set Method.....	3
1.4 The Governing Equations .....	6
1.5 Organization of the Thesis .....	7
CHAPTER 2: THE LEVEL SET METHOD.....	8
2.1 Advection of Level Set Function .....	8
2.2 Reinitialization of the Level Set Function .....	9
2.2.1 Second-order reinitialization.....	10
2.2.2 Fourth-order reinitialization.....	12
2.3 Numerical Tests of the Reinitialization Scheme.....	14
2.3.1 Reinitialization of a 2D exponential function.....	15
2.3.2 Circle deformation in a rotational velocity field.....	17
2.3.3 Conclusions.....	18
CHAPTER 3: THE MODIFIED RIEMANN-GHOST FLUID METHOD.....	21
3.1 The Riemann-Ghost Fluid Method (R-GFM).....	21
3.2 The Modified R-GFM.....	22
3.3 Correction to the Interfacial Normal Velocity .....	25
3.4 Area Fraction of the Interfacial Cells.....	26

3.5	Test Case: 2D Explosion Problem .....	28
CHAPTER 4: BLOCK-STRUCTURED MESH REFINEMENT .....		34
4.1	The block-structured adaptive mesh refinement.....	34
4.2	Prolongation and Restriction.....	36
4.3	Refinement criteria.....	36
4.4	An example on grid structure.....	39
CHAPTER 5: NUMERICAL EXAMPLES.....		41
5.1	1D Shock tube problems .....	41
5.1.1	Gas-gas shock interactions.....	41
5.1.2	Gas-water shock interactions .....	46
5.2	2D Shock bubble cases .....	47
5.2.1	Mach 1.22 air-helium shock bubble interaction.....	47
5.2.2	Air-R22 shock bubble interaction.....	54
5.2.3	Mach 1.43 water-air shock-bubble interaction: .....	56
5.2.4	The Richtmyer-Meshkov instability .....	63
CHAPTER 6: CONCLUSIONS.....		72
REFERENCES .....		74

## LIST OF TABLES

TABLE 2.1: Max norm of reinitialization error for a 2D cylindrical function.....	16
TABLE 2.2: Loss of mass at $t = 2.0$ for circle deformation problem (in %). .....	19
TABLE 5.1: Numerical Schlieren images of the density gradient for the air-helium shock bubble interaction simulation and comparison with results from [57]. .....	51
TABLE 5.2: Quantitative data during the transition stage of a 1Gpa water-air shock interaction, with comparison with the front tracking method [63] and grid-aligned GFM [18]. .....	59
TABLE 5.3 Density contours of the 2D Air-SF6 Richtmyer-Meshkov instability ( $dx/\lambda=1/256$ ). .....	67

## LIST OF FIGURES

FIGURE 1.1 Typical configuration of a 2D computational domain. ....	7
FIGURE 2.1: Computational stencil for the fourth-order reinitialization [30] of the first derivative of $\phi$ at point $x_i$ .....	14
FIGURE 2.2: Convergence rate corresponding to different fictitious time marching schemes for the second-order reinitialization scheme. ....	17
FIGURE 2.3: Interface contours at $t=1$ s for the circle deformation problem. ....	20
FIGURE 3.1: Construction of the interfacial Riemann problem for interfacial cell $P_A$ , using the R-GFM approach suggested in [17]. ....	22
FIGURE 3.2: The staircase effect observed in solutions obtained using the original R-GFM. ....	23
FIGURE 3.3: Construction of the cut-cell function for a given interfacial cell. ....	27
FIGURE 3.4: Six typical types of cut cells considered in IMPACT in 2D. ....	27
FIGURE 3.5: Flowchart for the modified R-GFM proposed in this work. Highlighted text in red indicate modifications from the original R-GFM. ....	30
FIGURE 3.6: Density profiles of a cylindrical shock propagation with two levels of mesh refinement. ....	31
FIGURE 3.7: Location of contact discontinuity for the cylindrical shock propagation problem using the R-GFM [17] and the modified R-GFM schemes. ....	32
FIGURE 3.8: Closeup view of the location of the contact discontinuity for the cylindrical shock propagation problem. ....	33
FIGURE 4.1: A typical block-structured mesh refinement process [43], with ‘Z-route’ labelling for child blocks. ....	35
FIGURE 4.2: Logic flowchart for two-criteria mesh refinement. ....	38
FIGURE 4.3: An example of recursive mesh refinement. ....	39
FIGURE 4.4: Grid structure showing adaptive mesh refinement for a 2D gas-water shock interaction problem. ....	40
FIGURE 5.1: Numerical solutions for 1D air-helium shock interactions at $t = 0.16$ . ....	44
FIGURE 5.2: Numerical solutions for 1D air-helium strong shock interactions at $t = 0.01$ . ....	45

FIGURE 5.3: Numerical solutions for 1D air-water shock interactions at $t = 0.24$ ms....	47
FIGURE 5.4: Problem setup for the shock bubble problem. ....	48
FIGURE 5.5: Time evolution of downstream, upstream and jet locations for Air-Helium shock bubble problem. ....	52
FIGURE 5.6: Numerical Schlieren images showing the time evolution of the air-helium shock bubble problem. Left panel: $427 \mu\text{s}$ , Middle panel: $674 \mu\text{s}$ , Right panel: $983 \mu\text{s}$ . (a) Second-order reinitialization (108 p.p.r.) (b) Second-order reinitialization (216 p.p.r.) (c) HJ-WENO reinitialization (216 p.p.r.). ....	53
FIGURE 5.7: Numerical Schlieren images of shock-induced R22 bubble collapse in air. ....	55
FIGURE 5.8: Numerical Schlieren images of the interaction between a 1 Gpa water shock and an air bubble.....	60
FIGURE 5.9: Closeup view of density gradient contours when water-hammer shock is formed: Comparison between different numerical schemes.....	61
FIGURE 5.10: Mass conservation errors for the 1.0 Gpa water shock impinging on an air bubble problem. ....	62
FIGURE 5.11: The computational domain and geometric parameters for Richtmyer-Meshkov instability simulation (not to scale). ....	63
FIGURE 5.12: Density contours from the Air-SF6 RMI simulation at (a) $\tau=5$ , $dx/\lambda=1/256$ , (b) $\tau=10$ , $dx/\lambda=1/256$ , (c) $\tau=5$ , $dx/\lambda=1/512$ , (d) $\tau=10$ , $dx/\lambda=1/512$ .....	66
FIGURE 5.13: Interface contours from the 2D Air-SF6 RMI simulation with fourth-order reinitialization of the level set function ( $dx/\lambda=1/256$ ) and (a) cubic interpolation and (b) quadratic interpolation. ....	68
FIGURE 5.14: (a) Spike and (b) bubble growth rates from simulations of the Air-SF6 RMI problem using the original and modified versions of R-GFM. ....	70
FIGURE 5.15: (a) Spike and (b) Bubble growth rates from IMPACT simulations using the modified R-GFM approach and showing convergence with respect to the mesh.....	71

## CHAPTER 1: INTRODUCTION

### 1.1 Objective

Multi-material compressible flows are observed in several applications of practical relevance including combustion [1, 2], cavitation [3, 4] and shock lithotripsy [5, 6]. In recent years, significant effort has been expended in solving the governing equations associated with such flows with increasing efficiency and accuracy. In particular, the use of Ghost Fluid Method (GFM) [7] and its derivatives to accurately obtain the fluid state on the interface have been adopted widely. However, certain drawbacks of the ghost fluid approach such as overheating errors [7, 8], and the appearance of unphysical oscillations of density and pressure [9, 10] are well known and have been documented in the literature. In addition, the Level Set Method (LSM) [11], which is often used as the interface-tracking scheme under the GFM, can also have a critical impact on the quality of multi-medium interface. Specifically, the area-conservation error and the accuracy of the interface can depend on the choice of different reinitialization approaches in the LSM [12, 13, 14]. In this thesis, modifications to the GFM have been proposed, and the following questions are investigated using a range of high-fidelity simulations:

1. *How do the different ghost fluid methods affect the numerical behavior of the solutions in simulations of multimediuim compressible flows?*

2. *To what extent do the reinitialization schemes of different orders of accuracy affect the quality of the multi-material interface in the simulation of compressible flows?*

To answer question 1, a cut-cell based ghost fluid method will be proposed in this thesis. *The above study will be conducted using IMPACT, an in-house CFD code developed to describe shock-driven, multi-material compressible flows.*

## 1.2 The Ghost Fluid Method

The definition of interfacial boundary conditions plays a key role in the accuracy of numerical simulations of multi-medium compressible flows. In the Original GFM (OGFM) [7] approach, a ghost region is defined as a band of cells across a multi-medium interface from the real flow region. Within the ghost region, pressure and velocity are extrapolated directly from the corresponding real fluid, while the density is defined through a procedure called an isobaric fix [7]. The OGFM, however can exhibit strong oscillations in pressure while misplacing wave and interface positions, when it is employed in solving multi-medium flows with large density/pressure differences [9]. A remedy for such issues was suggested in [9], where the ghost state is instead determined from solving a multi-medium Riemann problem across the interface. The solution to the Riemann problem is then copied to the interfacial cells before each fluid is advected. A series of variants to the GFM have been proposed in [9, 15, 16, 17, 18] and based on the above notions.

The above approaches involve converting the multidimensional interfacial Riemann problems into a 1D Riemann problem parallel to the interface. In particular, in the Riemann-GFM (R-GFM) [17] approach, the interfacial Riemann problem is strictly constructed along the normal direction to the interface. Implementations of R-GFM in simulating multimediuim compressible flows can be found in [17, 19]. In a recent study [20], the R-GFM was successfully extended to simulate 3D droplet evaporation with surface tension and viscosity. However, the R-GFM is only first-order accurate (as shown in the solution of a 2D Rayleigh bubble collapse problem [21]) and more dissipative compared with other approaches. For instance, when R-GFM is applied to solve a gas-gas shock bubble problem [17], the growth of the resulting interfacial instabilities are

dissipated to a larger extent when compared with corresponding solutions from the front-tracking method [22] or artificial diffusivity schemes [23]. In R-GFM, copying the interface solution to nearby Cartesian grids can also result in the misplacement of waves. In multi-dimensions, this behavior leads to the so-called ‘staircase effect’ [24].

In this work, an area-averaging procedure based on a cut-cell approach is introduced to be combined with the original R-GFM, and is qualitatively similar to the strategy proposed by Hu and Khoo [24]. The difference between the proposed approach and the strategy of [24] is that in multidimensions, the averaging procedure is applied to the normal velocity component only, while the tangential velocity component is still calculated through constant extrapolation. This ensures the free slip boundary condition is enforced at the multimedial interface. From the wide range of numerical tests reported in this thesis, we will show the modified R-GFM, when combined with a high-order level set approach [13] demonstrates improved performance in describing interfacial instabilities, while limiting mass conservation errors compared with the original R-GFM approach.

### 1.3 The Level Set Method

In numerical simulations of multi-medium compressible flows, the interface can be subjected to frequent topology changes and the emergence of topologically complex features such as sharp corners. The Level Set Method (LSM) [11] has been widely used in the simulation of flows with such complex features and involving interfaces separating multiple media. The LSM computes the interface as the zero level set of an implicit higher-dimensional function, that is forced to satisfy:

$$\phi(x, y): |\nabla\phi| = 1 \tag{1.1}$$

where  $\phi(x, y)$  is the level set function and  $\phi(x, y) = 0$  represents the multi-medium interface. In practice [25], solving the above level set advection equation within a narrow band of cells flanking the interface has been shown to be sufficient. Hence, compared with other sharp interface approaches, there are two major advantages to the level set approach:

1. Topology changes, such as mergers or break-up, are naturally expressed by the level set function without recourse to explicit interface tracking or reconstruction procedures.
2. Properties of the interface, such as the interface normal direction and curvature, can be easily computed as derivatives of the level set function.

The LSM (and GFM when coupled with it) requires the definition of  $\phi$  over a band of cells. In practice, a constant band width on either side of the interface can be achieved in time, by requiring  $\phi$  to be a signed distance function [26]. To maintain the level set function as a signed distance function, a reinitialization step is introduced in the solution scheme at every timestep, once the level set function is advanced by the external velocity field. The reinitialization equation used is given by [26],

$$\frac{\partial \phi}{\partial \tau} + \text{sgn}(\phi^0)(|\nabla \phi| - 1) = 0 \quad (1.2)$$

Here,  $\tau$  is a fictitious time, and the above equation is solved iteratively to steady state. Typically, the reinitialization equation is discretized with a third-order Runge-Kutta scheme [27] in time, and a fifth-order WENO scheme [28] in space, which is commonly referred to as the HJ-WENO discretization. Despite the use of high order schemes, implementations of the original HJ-WENO scheme have been shown to be first-order accurate in the interface error terms [29]. Since the spatial discretization of  $\phi$  does not

include information on the zero level set function, the computed interface can be shifted by up to one mesh width as the iterations reach steady state [12]. To resolve this issue, the authors of [12] suggested approximating the first derivative of  $\phi$  using the following equation:

$$D_x^+ \phi_i = \pm \frac{\phi_i}{|D_i|}, \quad \text{if } \phi_i \cdot \phi_{i\pm 1} < 0 \quad (1.3)$$

The distance from  $i^{\text{th}}$  grid to the interface  $D_i$ , is obtained from cubic interpolation. The above first-order upwind approximation is based on the fact that  $\phi = 0$  at the interface. As a result, the level set value adjacent to the interface will eventually converge to the signed distance of the interface.

Similarly, Min and Gibou [13] developed a second-order reinitialization approach, in which the distance  $D_i$  in equation (1.3) is computed using a quadratic interpolation. The scheme is also compatible with adaptive mesh refinement (AMR), and was shown to be third-order accurate near the interface and second-order accurate for both static and dynamic sharp interface problems. *This second-order reinitialization approach constitutes the primary reinitialization scheme employed in IMPACT.* To achieve higher order accuracy, Ch  n   et. al also developed a fourth-order reinitialization scheme [30], in which the intersection points between the interface and the Cartesian grid are approximated using cubic interpolants, while spatial derivatives are computed using fourth-order divided differences. However, it is not clear if the fourth-order scheme can be applied to highly dynamic problems, since the cubic interpolation might result in numerical oscillations, particularly in the presence of features such as kinks near the interface [13].

In addition to the above strategies, schemes that avoid the multimediuim interface being altered by the reinitialization have been suggested. For instance, Hu and Khoo proposed the I-GFM approach [8], in which the reinitialization process is applied only to non-interfacial cells. Terashima and Tryggvason merged the ghost fluid method with front tracking method [22], where the unknown normal vector on non-interfacial ghost cells are calculated through extrapolating the known normal vectors near the interface. As a result, the use of the level set function is avoided. Both schemes have been successfully applied in simulating gas-liquid compressible flows.

#### 1.4 The Governing Equations

The hyperbolic conservation form of the governing equations is used to describe each distinct fluid in this work. Consider a rectangular box filled with two fluids A and B (FIGURE 1.1). The governing equations are solved in conservation form:

$$\frac{\partial \mathbf{U}}{\partial t} + \frac{\partial \mathbf{F}}{\partial x} + \frac{\partial \mathbf{G}}{\partial y} = 0 , \quad (1.4)$$

$$\text{where } \mathbf{U} = \begin{pmatrix} \rho \\ \rho u \\ \rho v \\ E \end{pmatrix}, \mathbf{F} = \begin{pmatrix} \rho \\ \rho u^2 + p \\ \rho uv \\ (E + p)u \end{pmatrix}, \mathbf{G} = \begin{pmatrix} \rho \\ \rho uv \\ \rho v^2 + p \\ (E + p)v \end{pmatrix}.$$

In the above equation,  $\rho$  is the density,  $(u, v)$  are the fluid velocity components in the  $(x, y)$  directions respectively,  $p$  is pressure and  $E$  is the total energy. The problem is closed using the stiff gas equation of state,

$$p = \rho e(\gamma - 1) - p_\infty, \quad (1.5)$$

where  $e$  is the internal energy and  $p_\infty$  is the ambient pressure. In this work, the following material properties for water have been used:  $\gamma_w = 4.4, p_\infty = 6 \times 10^8 \text{ Pa}$ . In IMPACT,

spatial derivatives are obtained using fifth-order WENO reconstruction [31], while time integration is handled with a third-order TVD Runge-Kutta scheme [27]. For gas–gas multimediuim flows, the Roe-solver [32] is used to obtain numerical fluxes at the inter-cell boundaries, while the Lax-Friedrich solver [33] is used for gas-liquid flows.

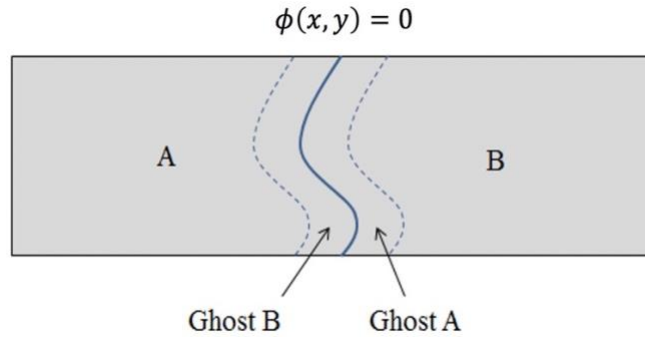


**FIGURE 1.1 Typical configuration of a 2D computational domain.**

## 1.5 Organization of the Thesis

This thesis is organized as follows: The level set method is described in greater detail along with a review of different high-order level set methods in Chapter 2. The accuracy of HJ-WENO, second-order and fourth-order reinitialization approaches are also verified with static and dynamic tests. The modified Riemann-GFM is introduced in Chapter 3, along with a simplified approach to approximate the area fraction of the cut-cell. In Chapter 4, the implementation of the block-structured mesh refinement toolkit PARAMESH to the multimediuim flow solver IMPACT is covered. Finally, the validation of the modified Riemann-GFM approach implemented in IMPACT using multiple test cases in 1D and 2D is described in Chapter 5. The major focus of this chapter is a comparison between the original R-GFM and the modified R-GFM, as well as the performance of different reinitialization schemes in simulating 2D gas–gas compressible flows. A summary of results and avenues for future work are discussed in Chapter 6.

## CHAPTER 2: THE LEVEL SET METHOD

The Level Set Method (LSM) is used to track the location of the multi-material interface in IMPACT. In the LSM approach [11], the interface is described implicitly by the signed distance function  $\phi$ , where  $\phi > 0$  and  $\phi < 0$  represent the distinct fluids in a two-fluid system, while  $\phi = 0$  represents the interface. In the interest of computational efficiency, the LSM uses flow variables (velocity and normal direction) from a band of cells that are adjacent to the interface. In this work, the band width was chosen to be  $6\Delta x$ , which was the band size employed in the implementation of the ghost fluid method as well.

### 2.1 Advection of Level Set Function

The level set approach is composed of an advection step and a reinitialization step. The equation that governs the motion of the interface is given by [11]:

$$\frac{\partial \phi}{\partial t} + \mathbf{U} \cdot \nabla \phi = 0, \quad (2.1)$$

where  $\mathbf{U}$  is the external velocity field. As suggested in [34], equation (2.1) can be written alternatively in terms of its motion in the normal direction as follows,

$$\frac{\partial \phi}{\partial t} + c U_n |\nabla \phi| = 0, \quad (2.2)$$

with

$$c = \begin{cases} 1, & \text{if } |\phi| \leq \beta \\ \frac{(|\phi| - \gamma)^2 (2|\phi| + \gamma - 3\beta)}{(\gamma - \beta)^3}, & \text{if } \beta < |\phi| < \gamma \\ 0, & \text{if } |\phi| > \gamma. \end{cases} \quad (2.3)$$

In equation (2.2),  $U_n$  is the projection of the external fluid velocity onto the interface normal direction, while the cutoff function  $c$ , is introduced to ensure a smooth transition between the inner ( $\beta = 3 dx$ ) and outer ( $\gamma = 6 dx$ ) regions of the computational band. Equation 2.2 is integrated in time in IMPACT using a third-order RK-TVD scheme [27], while a fifth-order WENO reconstruction to represent spatial derivatives [28]. The normal direction to the interface,  $\mathbf{n} = \nabla\phi/|\nabla\phi|$ , is computed using a fourth-order central finite difference scheme in IMPACT. Note that  $\nabla\phi$  is approximated by the Godunov-Hamiltonian scheme [26]:

$$|\nabla\phi| = H_G(\phi)$$

$$= \begin{cases} \sqrt{\max(|(D_x^{up}\phi)^+|^2, |(D_x^{down}\phi)^-|^2) + \max(|(D_y^{up}\phi)^+|^2, |(D_y^{down}\phi)^-|^2)}, & \text{if } U_n > 0 \\ \sqrt{\max(|(D_x^{up}\phi)^-|^2, |(D_x^{down}\phi)^+|^2) + \max(|(D_y^{up}\phi)^-|^2, |(D_y^{down}\phi)^+|^2)}, & \text{if } U_n \leq 0 \end{cases} \quad (2.4)$$

with  $(D)^+ = \max(D, 0)$  and  $(D)^- = \min(D, 0)$ .

## 2.2 Reinitialization of the Level Set Function

As the interface evolves, the level set function  $\phi$  may deviate from its initialization as a signed distance function. As a result, a reinitialization step is often required [26], after each timestep to ensure  $|\nabla\phi| = 1$ . In practice, this is enforced by iteratively solving the following equation to steady-state [26]:

$$\frac{\partial\phi}{\partial\tau} + \text{sgn}(\phi^0)(|\nabla\phi| - 1) = 0, \quad (2.5)$$

where the smoothed sign function  $sgn(\phi_0)$  is further defined as:

$$sgn(\phi^0) = \frac{\phi^0}{\sqrt{\phi^{0^2} + dx^2}} \quad (2.6)$$

The superscript  $\phi^0$  denotes the value of  $\phi$  at the first iteration. A typical choice for the fictitious time step  $d\tau$ , is  $d\tau = dx/2$  [34], since it has been observed to provide fast convergence rates for commonly used iterative schemes, while  $|\nabla\phi|$  is estimated from equation (2.4).

### 2.2.1 Second-order reinitialization

We briefly review the numerous approaches available to compute the reinitialization step of the level set calculation [12, 13, 35, 29]. A relatively simple strategy to solving equation (2.5) is to use the same discretization scheme in time and space as for the advection equation described in Section 2.1, an approach called the Hamilton Jacobi-WENO scheme (HJ-WENO) [26]. The HJ-WENO scheme is second-order accurate in approximating the zero level set function [30], and exhibits a tendency for the interface to move towards the adjacent Cartesian mesh [12]. To predict the interface location more accurately, Smereka [12] suggested that the location of zero level set should be included when calculating the first derivative of  $\phi$ . Although their scheme is first-order accurate at the interface, it achieves second-order accuracy globally.

In IMPACT, we adopt the reinitialization scheme proposed by Min and Gibou [13], who extended the above idea to second order accuracy at the interface on an adaptive mesh. In their framework, the first derivative of  $\phi$  inside the computational band (not adjacent to the interface) is estimated through the second-order divided difference:

$$D_x^+ \phi_i = \frac{\phi_{i+1} - \phi_i}{dx} - \minmod(D_{xx}\phi_i, D_{xx}\phi_{i+1}) \quad (2.7)$$

$$D_x^- \phi_i = \frac{\phi_i - \phi_{i-1}}{dx} + \minmod(D_{xx}\phi_i, D_{xx}\phi_{i-1}). \quad (2.8)$$

The second derivative  $D_{xx}^0 \phi_i$ , is approximated by the central difference scheme, provided that all cells inside the band are located on the finest grid. In the cells immediately adjacent to the interface, the approximation of the first derivative is slightly modified with the requirement that  $\phi = 0$  along the interfacial points [13]:

$$D_x^+ \phi_i = \frac{0 - \phi_i}{s_I} - \minmod(D_{xx}^0 \phi_i, D_{xx}^0 \phi_{i+1}) \quad (2.9)$$

$$D_x^- \phi_i = \frac{\phi_i - 0}{s_I} + \minmod(D_{xx}^0 \phi_i, D_{xx}^0 \phi_{i-1}) \quad (2.10)$$

Here,  $D_{xx}^0 \phi_{i+1}$  is used instead of  $D_{xx}^0 \phi_{s_I}$ , since the latter formulation causes instability when the interface moves too close to the nearby grid point [13].

The intersection between the interface and Cartesian grid,  $s_I$ , is captured through a quadratic interpolation of  $\phi^0$ . For an interface intersecting the horizontal mesh between points  $x_i$  and  $x_{i+1}$ , the quadratic function to approximate the interfacial location is given by [13]:

$$\phi^0(x) = c_2 x^2 + c_1 x + c_0, \quad (c_0, c_1, c_2) = \begin{cases} c_2 = \frac{1}{2} \minmod[D_{xx}^0 \phi_i, D_{xx}^0 \phi_{i+1}] \\ c_1 = (\phi_{i+1}^0 - \phi_i^0)/dx \\ c_0 = (\phi_{i+1}^0 + \phi_i^0)/2 - c_2 dx^2/4 \end{cases} \quad (2.11)$$

The origin of the cut-cell function,  $\phi^0(x)$ , is located at the midpoint between  $x_i$  and  $x_{i+1}$ . When  $|c_2| < 10^{-6}$ ,  $s_I$  is computed assuming the interface cuts linearly through the grid,

i.e.  $s_I = dx/2 - c_0/c_1$ . Higher order schemes, such as the unidirectional cubic interpolation are an alternative in some cases [30]. However, the quadratic interpolation demonstrates better stability when there is a kink near the interface [13] and it is therefore used as the primary interpolation scheme to capture the intersection between the interface and the numerical mesh in IMPACT.

For the above iterative scheme to be stable, it has been shown that the fictitious step size for the interfacial grids  $d\tau$ , should be selected based on the location of the intersection [12, 13]:

$$d\tau = \min(dx, dy, s_{I_x}, s_{I_y})/2. \quad (2.12)$$

Since a steady-state solution is pursued, it is feasible to use an adaptive step size for grids at different locations. For non-interfacial points, we still choose  $d\tau = dx/2$ . Compared with using a globally uniform  $d\tau$ , applying the adaptive step size can increase the convergence rate of the iterations considerably (this improvement is demonstrated in Section 2.3.1).

### 2.2.2 Fourth-order reinitialization

The fourth-order reinitialization scheme of Ch  n   [30] has also been implemented in IMPACT, and is described here briefly. When compared with the second-order scheme discussed in § 2.2.1, this scheme uses fourth-order divided difference to approximate the one-sided first derivative. The corresponding upwind/downwind scheme for the first derivative of  $\phi$  is:

$$D_x^\pm \phi(x_i) = D_{-\frac{1}{2} \pm \frac{1}{2}}^1 + \text{MinMod}(D_{\pm 1}^2, D_0^2) * (x_i - x_{i \pm 1}) + a_\pm, \quad (2.12)$$

where

$$a_{\pm} = \begin{cases} (x_i - x_{i\pm 1}) * (x_i - x_{i\pm 2}) * \text{MinAbs}\left(D_{\frac{1}{2}\pm\frac{1}{2}}^3, D_{\frac{1}{2}\pm\frac{3}{2}}^3\right) & \text{if } |D_{\pm 1}^2| < |D_0^2| \\ (x_i - x_{i\pm 1}) * (x_i - x_{i\mp 1}) * \text{MinAbs}(D_0^3, D_1^3) & \text{if } |D_{\pm 1}^2| > |D_0^2| \end{cases}.$$

The first-order approximation for derivative  $D_k^m$  at point  $x_i$  is defined as:

$$D_k^m = \begin{cases} \frac{D_k^{m-1} - D_{k-1}^{m-1}}{x_{i+k+1} - x_{i-k-1+m}} & \text{if } m > 0 \\ \phi(x_{i+k+1}) & \text{if } m = 0 \end{cases}.$$

The corresponding seven-point computational stencil for the spatial derivative at point  $x_i$ , is shown in FIGURE 2.1. If the distance between the interface and the Cartesian grid is less than  $3dx$  in the horizontal direction, the intersection point will be included in the computational stencil.

Note that in the fourth-order scheme, it is difficult to apply the stabilizer for the second-derivative, as was done in equations (2.9) and (2.10). This is because in equation (2.9), the interface information is stored in the first term, namely  $\frac{0-\phi_i}{s_l}$ . If the grid is not adjacent to the interface, but still located inside the computation stencil (e.g., FIGURE 2.1), substituting  $D_{\frac{1}{2}\pm\frac{1}{2}}^1$  in equation (2.12) will result in a loss of the interface information. As a result, the fourth-order scheme will become unstable when the interface moves too close to the mesh.

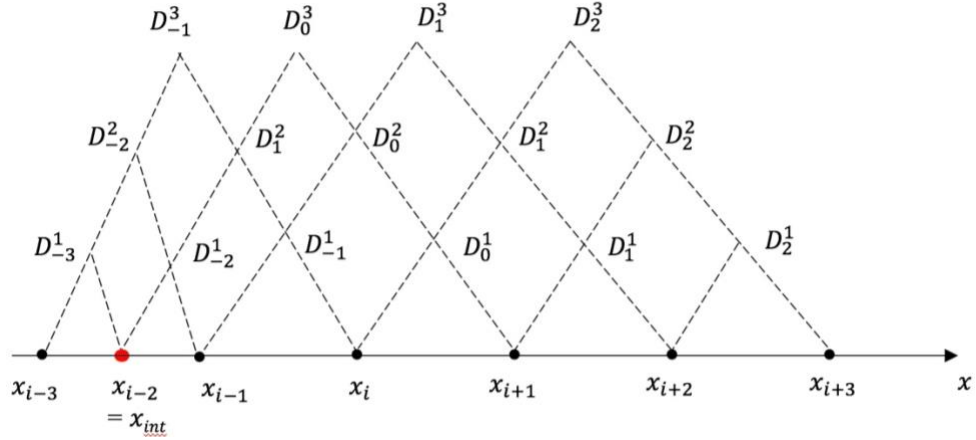


**FIGURE 2.1: Computational stencil for the fourth-order reinitialization [30] of the first derivative of  $\phi$  at point  $x_i$ .**

### 2.3 Numerical Tests of the Reinitialization Scheme

The accuracy and efficiency of different reinitialization methods implemented in IMPACT were investigated with static and dynamic test problems. The dynamic case, in particular, demonstrates the capability of different reinitialization schemes in preserving the interface information, when the interface is subjected to a vortical velocity field, which frequently occurs in simulations of real-flow applications. The evaluation of the different reinitialization schemes when coupled with more complicated external flow fields is presented in Chapter 5. The major focus in this section is to demonstrate the order of accuracy of these reinitialization schemes. All the simulations have been performed with the adaptive mesh refinement toolkit PARAMESH that was implemented in IMPACT as part of this thesis work. While the finest refinement level in the simulations may vary, the coarsest mesh was fixed at  $1/32$ .

### 2.3.1 Reinitialization of a 2D exponential function

Consider the square domain  $\Omega = [0,2]^2$ , in which the initial level set function before reinitialization is given by:

$$\phi^0(x, y) = \exp\left(\sqrt{(x-1)^2 + (y-1)^2} - 0.2313\right) - 1 \quad (2.12)$$

As the iterations proceed,  $\phi$  will asymptote to a signed distance function on  $\Omega$  (since the zero level set  $\phi^0(x, y) = 0$  is a function of a circle, the initial exponential function is eventually shaped into a cone). The simulation was stopped after 200 iterations. The mesh convergence of the max norm of error of  $\phi$  near the interface ( $|\phi(x, y)| < 1.2dx$ ) is reported in TABLE 2-1. The max norm of error  $L_\infty$ , is defined as,

$$L_\infty = \max_{|\phi(x,y)| < 1.2dx} |\phi(x, y) - \phi_{exact}(x, y)| \quad (2.12)$$

As indicated by the numerical results, the HJ-WENO reinitialization is second-order accurate for this case. The nominally second order reinitialization scheme on the other hand, demonstrates third order accuracy near the interface, which is reported in the literature [13] as well.

FIGURE 2.2 shows the convergence rate for the second-order scheme with different fictitious step sizes, where the finest mesh for the problem was  $dx = 1/128$ . From the plot, the adaptive time marching scheme requires fewer than 10 steps to reach steady state, although the convergence rate could depend on the complexity of the  $\phi$  function prior to reinitialization [13]. The uniform step size, in contrast requires greater than 100 iterations to achieve steady state. For dynamic cases, where the reinitialized level set function was shifted by a small amount after each RK-3 sub-step, around 5 steps were required for the iterations to reach steady state. As a consequence, using an adaptive fictitious step size for

the second-order reinitialization can achieve faster convergence rate than using a constant one.

**TABLE 2.1: Max norm of reinitialization error for a 2D cylindrical function.**

$N_x \times N_y$	$L_\infty$	Order of Accuracy
$32^2$	$3.60 \times 10^{-5}$	
$64^2$	$7.30 \times 10^{-6}$	2.30
$128^2$	$1.95 \times 10^{-6}$	1.90
$256^2$	$3.71 \times 10^{-7}$	2.39

**(a) HJ-WENO reinitialization**

$N_x \times N_y$	$L_\infty$	Order of Accuracy
$32^2$	$3.02 \times 10^{-3}$	
$64^2$	$4.63 \times 10^{-4}$	2.71
$128^2$	$5.70 \times 10^{-5}$	3.02
$256^2$	$7.48 \times 10^{-6}$	2.93

**(b) Second-order reinitialization**

$N_x \times N_y$	$L_\infty$	Order of Accuracy
$32^2$	$1.55 \times 10^{-4}$	
$64^2$	$1.10 \times 10^{-5}$	3.81
$128^2$	$4.70 \times 10^{-7}$	4.54
$256^2$	$6.32 \times 10^{-8}$	2.89

**(c) Fourth-order reinitialization**

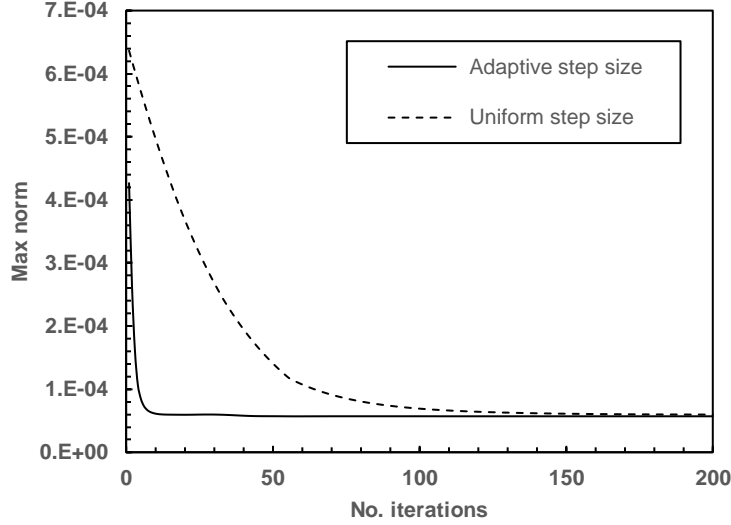


**FIGURE 2.2: Convergence rate corresponding to different fictitious time marching schemes for the second-order reinitialization scheme.**

### 2.3.2 Circle deformation in a rotational velocity field

A circle of radius 0.15 is placed at (0.5, 0.75) in the 2D square domain  $\Omega = [0,1]^2$ , and embedded in an external velocity field defined as follows:

$$u(x, y) = -\sin^2(\pi x)\sin(2\pi y) \quad (2.13)$$

$$v(x, y) = \sin^2(\pi y)\sin(2\pi x) \quad (2.14)$$

The RK3-TVD scheme is used for time integration for this case, with a fixed time step size of  $dt = dx_{finest}/2$ . In [13], the authors suggested using a second-order, semi-Lagrangian scheme for the advection equation. Although the scheme is unconditionally stable, it is less accurate and is more computationally expensive, since a bilinear interpolation is required for obtaining the departure point of the cartesian grid at each time step. For computational efficiency, adaptive mesh refinement was employed, where the coarsest mesh size for all cases was  $dx = 1/32$  (all the grids within the band for advection equation were refined to the finest level).

Results from this set of simulations are shown in FIGURE 2.3, and summarized in TABLE 2.2. The circle evolves in time by stretching and deforming under the influence of the imposed background velocity field. For  $t > 1.0$ , the direction of the velocity field was reversed in the simulations. The interface contour at  $t = 1.0$  is plotted at different mesh resolutions in FIGURE 2.3. It is clear that the fourth-order reinitialization scheme is capable of preserving more details of the head and tail structures of the interface, compared with the second-order reinitialization and the HJ-WENO schemes. In addition, the fourth-order scheme is associated with the least mass conservation errors at all mesh resolutions (as shown in TABLE 2.2). Both the second-order reinitialization scheme and the traditional HJ-WENO scheme display second-order accuracy in mass conservation. However, at  $t = 1.0$ , the second-order reinitialization predicts the location of head and tail more accurately than the HJ-WENO reinitialization, according to FIGURES 2.3 (a) and (b).

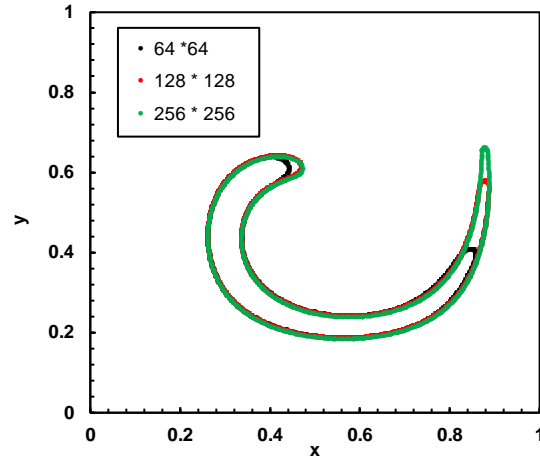
### 2.3.3 Conclusions

The performance of three reinitialization schemes, which are commonly used to maintain the level set function as the signed distance, is examined in this chapter. As demonstrated by the numerical tests, the fourth-order reinitialization scheme [30] is the most accurate in limiting the area-conservation error and predicting the location of the interface. The second-order reinitialization [13] and the HJ-WENO reinitialization [26] show comparable performance in solving a 2D dynamic problem. In contrast, the second-order reinitialization is able to reach third-order accuracy locally when used to solve a 2D static problem, whereas the HJ-WENO reinitialization is only second-order accurate near the interface.

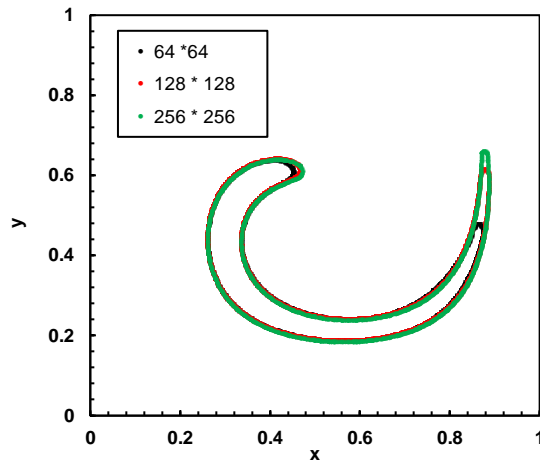
**TABLE 2.2: Loss of mass at  $t = 2.0$  for circle deformation problem (in %).**

	$64^2$	$128^2$	$256^2$
HJ-WENO (Order of Accuracy)	21.6 –	4.50 (2.26)	1.00 (2.17)
Second-order (Order of Accuracy)	15.4 –	3.47 (2.15)	0.96 (1.85)
Fourth-order (Order of Accuracy)	-6.73 –	-0.681 (3.3)	0.012 (5.8)

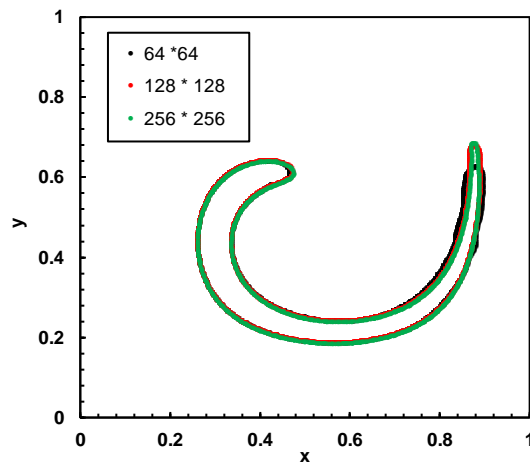
(\* Negative sign indicates a gain in area)



(a) HJ-WENO reinitialization



(b) Second-order reinitialization



(c) Fourth-order reinitialization

FIGURE 2.3: Interface contours at  $t=1$  s for the circle deformation problem.

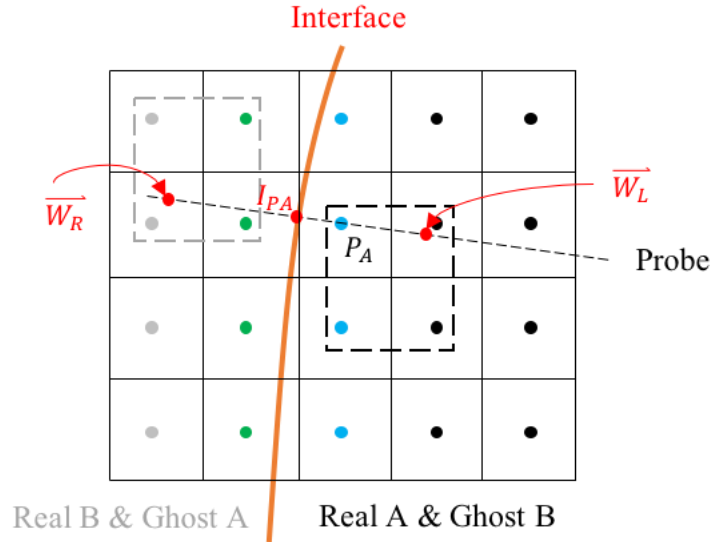
## CHAPTER 3: THE MODIFIED RIEMANN-GHOST FLUID METHOD

### 3.1 The Riemann-Ghost Fluid Method (R-GFM)

In IMPACT, the Ghost Fluid Method (GFM) is used to enforce the boundary conditions at a multi-medium interface. Consider a two-fluid (material A and material B) Riemann problem; the Original GFM (OGFM) separates the computational domain into two regions, and treats each material individually through the introduction of a ghost fluid [7]. For computations involving material A, the domain occupied by material B is replaced with a ghost region which has the same equation of state as material A: the pressure and the normal velocity inside the ghost region are copied directly from material B, while the entropy is defined through a constant extrapolation from the region containing material A across the interface [7]. Since wave structures obtained from single-medium, real-ghost configurations do not always correspond to the two-medium interactions of interest, incorrect interface locations and strong oscillations in the pressure wave are observed when the OGFM is used to solve strong shock interaction problems [9].

An alternative approach that mitigates the above issues is the Riemann Ghost Fluid Method (R-GFM) suggested in [17]. In the R-GFM approach, the state of fluid (density, normal velocity and pressure) on the interface, is obtained directly from solving a multi-medium Riemann problem before being extrapolated across the interface. The Riemann problem is constructed across the interface by defining a numerical ‘*probe*’ in the interface-normal direction (FIGURE 3.1). Then, the ‘*left*’ and ‘*right*’ states for the Riemann problem are obtained from interpolation to points located at a distance  $1.5\Delta x$  from the interfacial point and along the direction of the probe. From the exact solution to the interfacial

Riemann problem, the star states are obtained and copied to the interfacial grid points, while the ghost cells are populated using a constant extrapolation approach.



- Real cell for fluid A
- Real Interfacial cell for fluid A
- Ghost Interfacial cell for fluid A
- Ghost cell for fluid A

**FIGURE 3.1: Construction of the interfacial Riemann problem for interfacial cell  $P_A$ , using the R-GFM approach suggested in [17].**

### 3.2 The Modified R-GFM

Early simulation results of gas-gas compressible flows [17, 19] have shown the R-GFM numerical scheme can result in inaccuracies in multi-medium problems. For instance, the growth rate of the Richtmyer-Meshkov instability is underpredicted by the original R-GFM [10], and when compared with other numerical schemes [36, 22]. A common issue associated with GFM-related correction techniques stems from copying the solution to the

interfacial Riemann problem to the nearby interfacial cells, which can result in the misplacement of waves associated with the solution, and in oscillations of the interface (referred as the ‘stair steps’ effect [24]). FIGURE 3.2 demonstrates the ‘stair steps’ effect observed in simulations using the R-GFM scheme. Consider two fluids in a rectangular domain separated by an inclined interface as shown. The ‘left’ and ‘right’ states of the interface are uniformly defined as  $\mathbf{W}_{L/R}$  ( $\mathbf{W} = \{\rho, U_n, p\}$ ) initially. If the resulting wave structure from solving the interfacial Riemann problem is a rarefaction wave, the same solution is assigned to all interfacial points on one side of the interface, e.g. for points  $P_1$ ,  $P_2$  in FIGURE 3.2,  $\mathbf{W}_{IP1L}^* = \mathbf{W}_{IP2L}^*$ . However, the solution states at  $P_1$  and  $P_2$  should be treated differently, since their distances to the interface are not identical. If the solution satisfies  $\mathbf{W}_{IP1L}^* > \mathbf{W}_L$ , copying the interfacial star state to its corresponding interfacial cell point results in an overestimation of the real state [FIGURE 3.2 (b)].

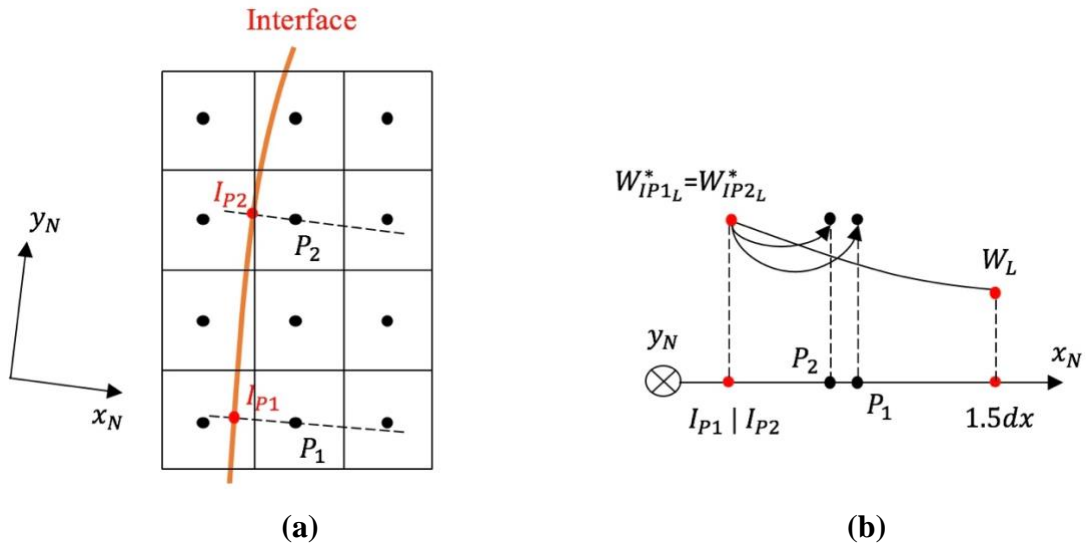


**FIGURE 3.2: The staircase effect observed in solutions obtained using the original R-GFM.**

Following [24], we propose the correction step in the original R-GFM should be applied only to the ghost portion of the interfacial cell, while the real portion of the interfacial cell is unaffected by the R-GFM fix. Since  $\mathbf{W}_p$  denotes the geometric average between the real state and the ghost state inside interfacial cell  $P$ , we propose the following refined correction technique applied to the interfacial cells:

$$\mathbf{W}_{new} = \alpha_{real}\mathbf{W}_{real} + (1 - \alpha_{real})\mathbf{W}_{ghost}, \quad (3.1)$$

with 
$$\alpha_{real} = \frac{\text{Area of the real fluid region of a cut-cell}}{dx \cdot dy} \quad (3.2)$$

Here  $\alpha_{real}$  is the area fraction of the real fluid portion of an interfacial cell,  $\mathbf{W}_{real}$  is the state of the interfacial cells before applying the R-GFM fix, and  $\mathbf{W}_{ghost}$  is the state of ghost region obtained from the original-RGFM approach.

A significant difference between the above proposed approach and the original R-GFM scheme [17] is that in our scheme, the correction step is applied to both the real interfacial cells and the ghost interfacial cells, whereas in the original R-GFM approach the correction is applied only to the real interfacial cells. As a result, different definitions of  $\mathbf{W}_{ghost}$  are used in real and ghost interfacial cells – in real interfacial cells,  $\mathbf{W}_{ghost}$  is populated with star state values obtained from the exact Riemann solver, while the ghost interfacial cell values of  $\mathbf{W}_{ghost}$  are populated with primitive variables obtained through constant extrapolation. Note that the real region corresponding to a ghost interfacial cell is normally undefined at the beginning of the simulation. However, for the correction technique above to be valid, the interfacial ghost cells, which include a portion of the real region must be defined through a one-layer extrapolation initially.

### 3.3 Correction to the Interfacial Normal Velocity

In GFM, the free-slip boundary condition is enforced at the multi-material interfaces [7]. Applying equation (3.1) directly to the vertical/horizontal component of the velocity will violate such a condition. As a result, we only perform the area averaging correction on the normal component of the interfacial velocity. In practice, once the velocity field on the ghost region is defined through extrapolation, the normal component of the vertical/horizontal velocity is replaced with the area-averaged value, i.e.,

$$u_{new} = u_{ghost} - \left| \mathbf{U}_{n_{ghost}} \right| n_x + \left| \mathbf{U}_{n_{new}} \right| n_x \quad (3.2)$$

Here  $n_x$  is the horizontal component of the unit normal to the interface.  $|\mathbf{U}_n|$  is the magnitude of the interfacial normal velocity, which satisfies the following,

$$|\mathbf{U}_n| = n_x u + n_y v \quad (3.3)$$

The averaged normal velocity  $\mathbf{U}_{n_{new}}$ , is obtained in the same manner as described by equation (3.1). Combining equations (3.1) and (3.2), the horizontal component of the interfacial velocity can be further expressed as followed,

$$u_{new} = u_{ghost} + n_x \alpha_{real} \left( \left| \mathbf{U}_{n_{real}} \right| - \left| \mathbf{U}_{n_{ghost}} \right| \right). \quad (3.4)$$

The vertical component of the interfacial velocity can be obtained similarly. The above correction scheme is summarized in the flow chart shown in FIGURE 3.5. Compared with the original R-GFM [17], the modified scheme proposed here requires more memory, and is computationally more expensive.

### 3.4 Area Fraction of the Interfacial Cells

The level set based cut cell method has been successfully used in the numerical simulations of both compressible and incompressible flows [37, 38, 39]. In these methods, the area fraction of the interfacial cells  $\alpha$ , is calculated assuming the interface cuts through the cell linearly. The linear interface cut cell function,  $y = f(x)$  (with the origin located at the cell center, as shown in FIGURE 3.3), can be represented using a point on the curve  $(-\phi_P n_x, -\phi_P n_y)$  and the slope  $(-\frac{n_x}{n_y})$ :

$$\frac{y + \phi_P n_y}{x + \phi_P n_x} = \frac{-n_x}{n_y}. \quad (3.4)$$

From the cut cell function, the corresponding intercepts on the cell borders are obtained as  $A: (f^{-1}(\frac{dy}{2}), \frac{dy}{2}), B: (-\frac{dx}{2}, f(-\frac{dx}{2})), C: (f^{-1}(-\frac{dy}{2}), -\frac{dy}{2}), D: (\frac{dx}{2}, f(\frac{dx}{2}))$  In IMPACT, six different types of cut cells are considered and shown in FIGURE 3.4. With the intersection points known, the minor area portion of an interfacial cell,  $\alpha: (\alpha < \frac{1}{2})$ , can be computed from simple geometric calculations, i.e.

$$\alpha = \begin{cases} \frac{1}{2} \left( \frac{dx}{2} + x_A \right) \left( \frac{dy}{2} - y_B \right), & \text{if } |x_A| < \frac{dx}{2} \text{ and } |y_B| < \frac{dy}{2} \\ \frac{1}{2} \left( \frac{dx}{2} - x_A \right) \left( \frac{dy}{2} + y_D \right), & \text{if } |x_A| < \frac{dx}{2} \text{ and } |y_D| < \frac{dy}{2} \\ \frac{1}{2} \left( \frac{dx}{2} + x_C \right) \left( \frac{dy}{2} - y_D \right), & \text{if } |x_C| < \frac{dx}{2} \text{ and } |y_D| < \frac{dy}{2} \\ \frac{1}{2} \left( \frac{dx}{2} - x_C \right) \left( \frac{dy}{2} + y_B \right), & \text{if } |x_C| < \frac{dx}{2} \text{ and } |y_B| < \frac{dy}{2} \\ (dx - |x_A + x_C|) \frac{dy}{2}, & \text{if } |x_A| < \frac{dx}{2} \text{ and } |x_C| < \frac{dx}{2} \\ (dy - |y_B + y_D|) \frac{dx}{2}, & \text{if } |y_B| < \frac{dy}{2} \text{ and } |y_D| < \frac{dy}{2} \end{cases} \quad (3.5)$$

and

$$\alpha_{real} = \begin{cases} \alpha, & \text{for ghost interfacial cells} \\ 1 - \alpha, & \text{for real interfacial cells} \end{cases} \quad (3.6)$$

For the interfacial real cell which is not intercepted by the interface (i.e.  $\alpha_{real} = 1$ ), the correction step in the original R-GFM will not be applicable, although it is still involved in solving for the interfacial star state. Similar criteria for correction are applied to the interfacial ghost cell where  $\alpha_{real} = 0$ .

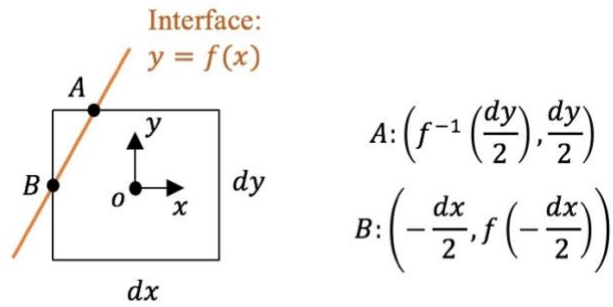


**FIGURE 3.3: Construction of the cut-cell function for a given interfacial cell.**

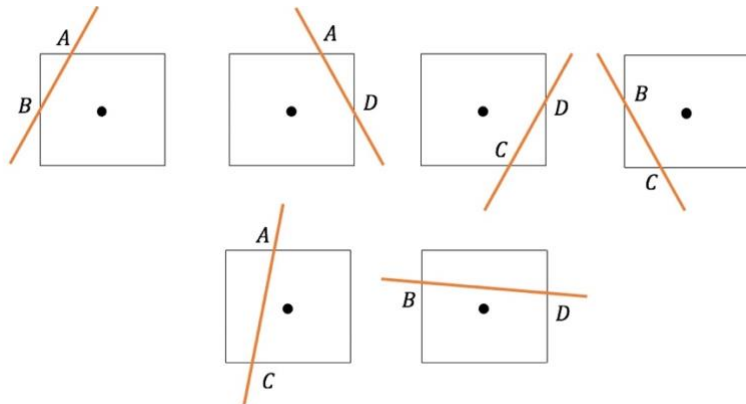


**FIGURE 3.4: Six typical types of cut cells considered in IMPACT in 2D.**

### 3.5 Test Case: 2D Explosion Problem

The 2D axisymmetric explosion problem is a useful test case to demonstrate the ‘stair steps’ effect observed in the GFM and its remediation using the above correction. The initial state of the problem [33] is defined as:

$$\begin{aligned}
 (\rho, u, v, p) = & \\
 \left\{ \begin{array}{ll} 1.0, 0.0, 0.0, 1.0, & \text{for } \sqrt{(x - 0.5)^2 + (y - 0.5)^2} < 0.2 \\ 0.125, 0.0, 0.0, 0.1, & \text{(elsewhere)} \end{array} \right. & (3.7)
 \end{aligned}$$

The contact discontinuity has been treated with the ghost fluid method, although the problem comprises a single material. For computational efficiency, two levels of adaptive mesh refinement with the finest mesh being  $\Delta x = 1/256$  were used. The mesh is relatively coarse, so that numerical errors are easier to observe. The second order reinitialization scheme is adopted to smooth the level-set function near the interface.

FIGURES 3.6 – 3.8 show the 3D view, 2D slices and closeup views respectively of the interface position at  $t = 0.25$  of the 2D explosion test problem, where the interface (contact discontinuity) has been approximated through a cubic interpolation of the level set function. As the initial interface is axisymmetric, the shock wave should propagate strictly outward as a circle. However, the staircase effect is clearly observed in the R-GFM simulation, especially at locations where the interface is parallel to the horizontal or the vertical axis. Similar oscillations in the waves and interface were also reported in the OGFM [40]. In contrast, the interface appears smoother when computed using the modified R-GFM [FIGURE 3.7 (b)]. Oscillations in the density are similarly dampened by the modified R-GFM scheme, as shown in FIGURE 3.6. Moreover, even at the coarser

resolution of  $N_x = 128$  used here, the modified R-GFM reproduces smoother density distributions when the results are compared with reported results of the OGFM computed with  $N_x = 200$  in [40].

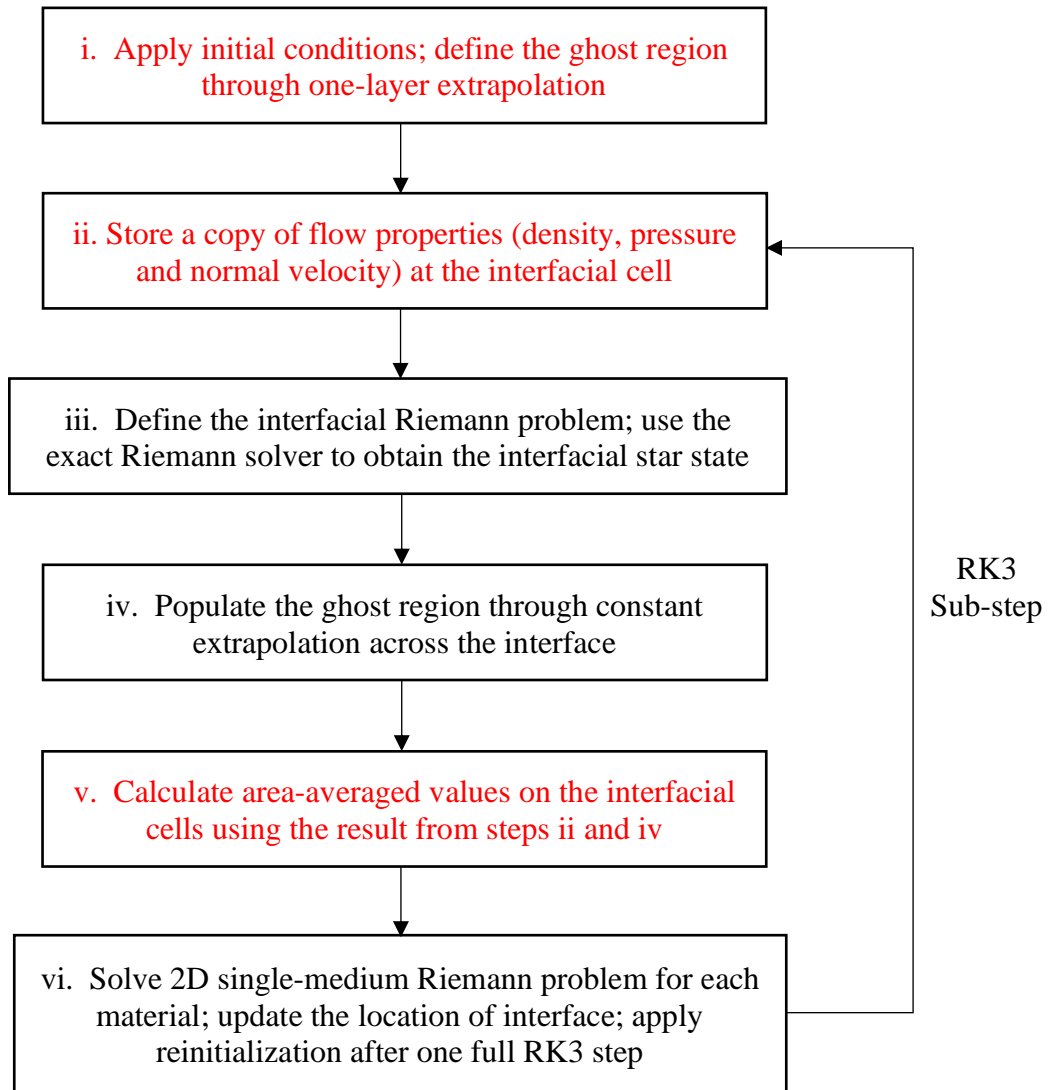
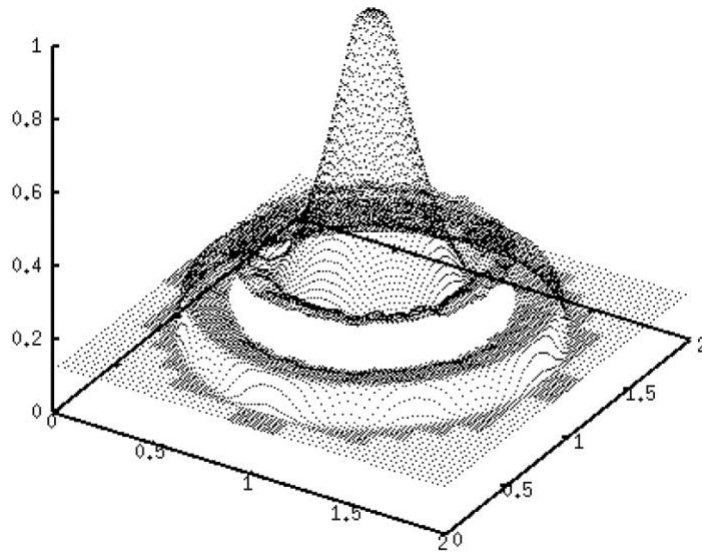
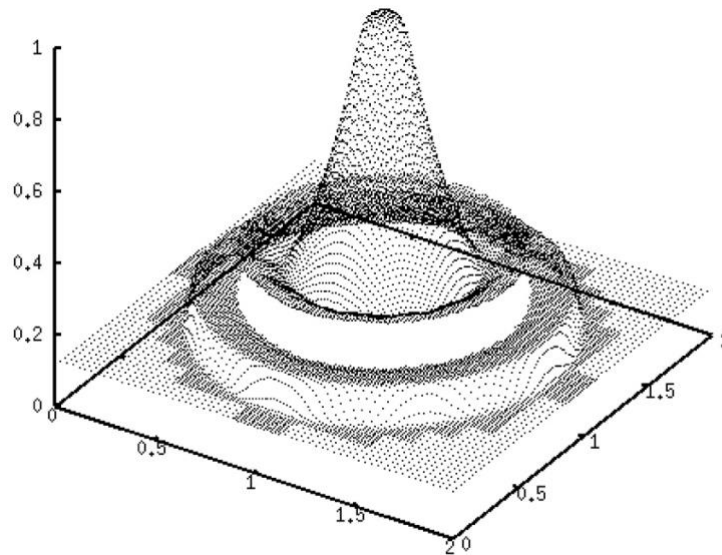


**FIGURE 3.5: Flowchart for the modified R-GFM proposed in this work. Highlighted text in red indicate modifications from the original R-GFM.**

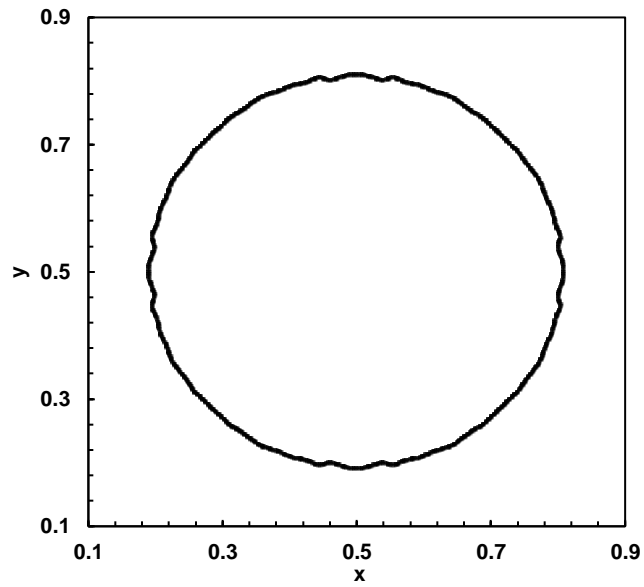


(a) Original R-GFM

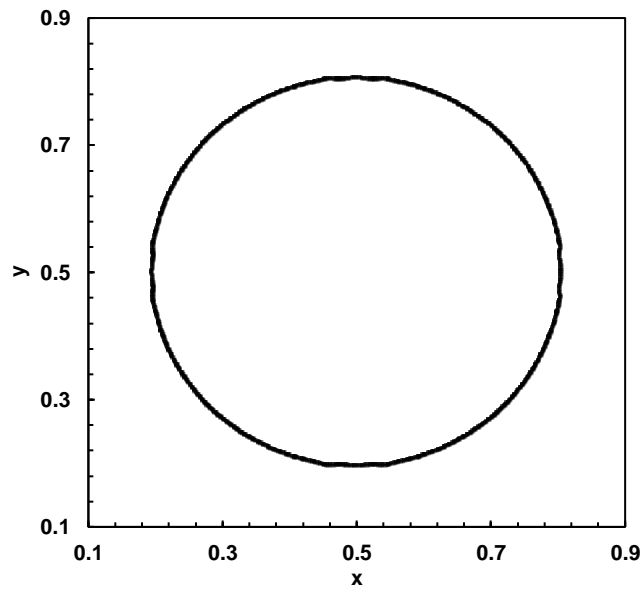


(b) Modified R-GFM

**FIGURE 3.6: Density profiles of a cylindrical shock propagation with two levels of mesh refinement.**

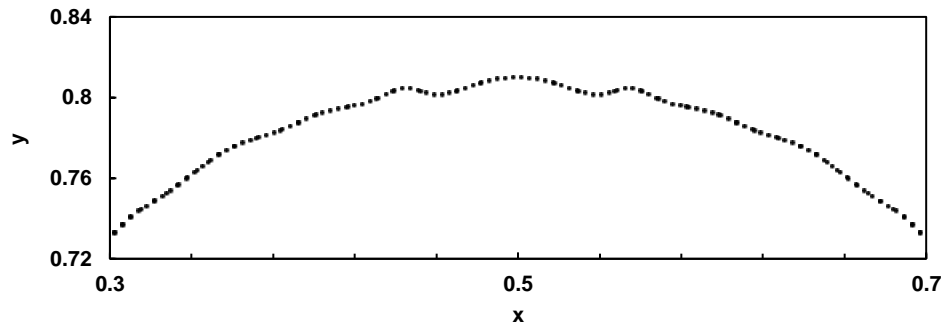


(a) Original R-GFM

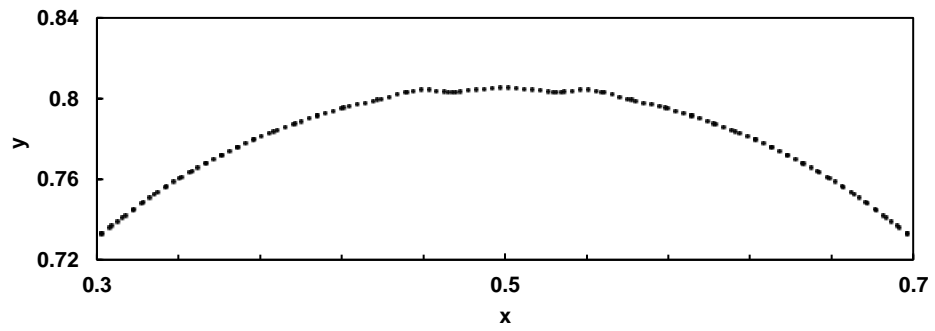


(b) Modified R-GFM

**FIGURE 3.7: Location of contact discontinuity for the cylindrical shock propagation problem using the R-GFM [17] and the modified R-GFM schemes.**



(a) Original R-GFM



(b) Modified R-GFM

**FIGURE 3.8: Closeup view of the location of the contact discontinuity for the cylindrical shock propagation problem.**

## CHAPTER 4: BLOCK-STRUCTURED MESH REFINEMENT

The adaptive mesh refinement (AMR) has been a popular choice to reduce the computational cost associated with simulating compressible flows and has been implemented in IMPACT. To resolve the fluid motion adequately, a fine mesh is used only in regions with sharp gradients in the solution field. The use of AMR to solve compressible flows was first suggested by Berger [41]. Subsequently, numerous variations on AMR approaches have been developed and reported in [42, 43, 44, 45]. In IMPACT, the block-structured AMR toolkit PARAMESH [43, 46, 47], is used for mesh refinement and integrated with the flow solver. When used in a parallel computation, PARAMESH [43, 46, 47] also enforces load balancing between the different processors. To further adapt PARAMESH for multi-medium compressible flows, the duo-criteria refinement is adopted.

### 4.1 The block-structured adaptive mesh refinement

PARAMESH employs a block-structured meshing framework in which the mesh is defined in terms of  $N$  by  $N$  (in 2D) so-called ‘blocks’, that are aligned with the grid. Simulations in PARAMESH are initialized with one block, and mesh refinement leads to a hierarchical block structure using a quad-tree structure in 2D, or an oct-tree structure in 3D [43]. When field variables within a block satisfy the criteria for refinement, the parent block is evenly divided into four child blocks, each with half the size of the parent block, while the mesh number is maintained the same. Similarly, if all four child blocks meet the de-refinement criteria, they are merged into their parent block and subsequently removed. At each time step, the refinement and de-refinement procedures are performed recursively, until all blocks are properly nested.

FIGURE 4.1 illustrates an example of the process of refinement of a block-structured mesh. Consider a portion (bottom left in FIGURE 4.1 (a)) of the computational domain that meets the refinement criteria, where the refinement levels are set to 2 to 4. This will lead to the eventual distribution of blocks shown in FIGURE 4.1(b). A total of 10 child blocks are generated in this case, where the grid spacing on the finest blocks (3, 4, 5, 6) are each  $dx_{finest} = dx_{initial}/2^3$ . In addition, all blocks are labelled according to ‘Morton’s Z-route’ rule [48], i.e., all child blocks which belong to the same parent block are labelled sequentially in a ‘Z’ shape, a strategy that makes it easier to identify neighboring blocks.

In IMPACT, the grid size of each block is chosen as  $(4 \times 4)$ . The block size cannot be less than the number of boundary guard cells, which ensures no extra communication is needed to update the boundary cells. Consequently, a larger block size will result in a larger buffer zone between the fine and coarse meshes, which is less memory efficient. Compared with the traditional AMR approaches, the blocked-structured refinement demands more memory, although the memory overhead is usually  $< 30\%$  [43].

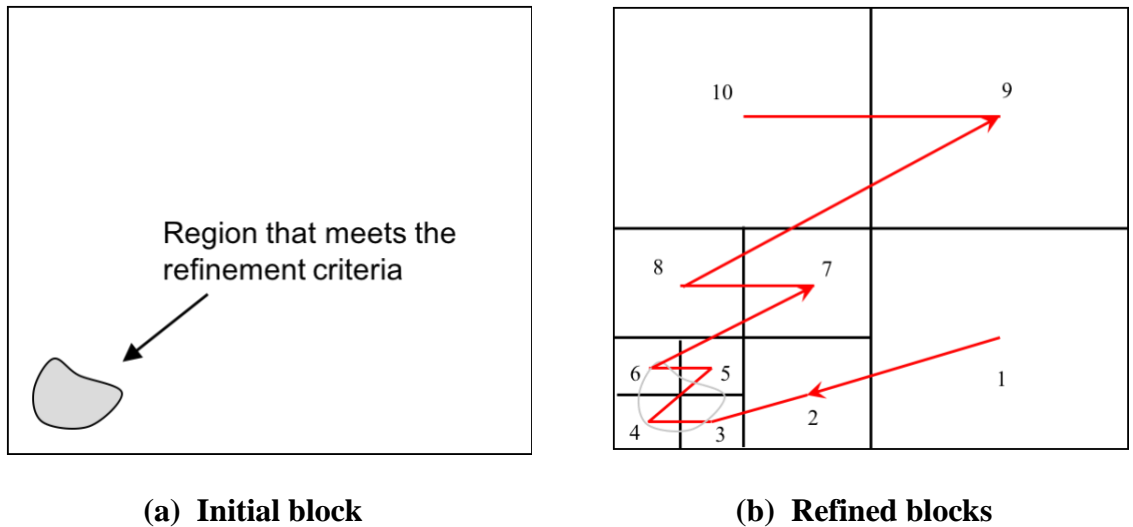


**FIGURE 4.1: A typical block-structured mesh refinement process [43], with ‘Z-route’ labelling for child blocks.**

## 4.2 Prolongation and Restriction

Once the new blocks are formed, restriction (fine to coarse) and prolongation (coarse to fine) operators are used to map the physical variables onto the new blocks. An arithmetic average is used for the restriction operators in IMPACT, where the conservative variables on a parent block,  $U_{(x,y)}^{parent}$  are constructed in 2D as follows:

$$U_{(x,y)}^{parent} = \frac{1}{4} \left( U_{(x+dx,y+dy)}^{child} + U_{(x-dx,y+dy)}^{child} + U_{(x+dx,y-dy)}^{child} + U_{(x-dx,y-dy)}^{child} \right) \quad (4.1)$$

To prolong the data from a coarse mesh to a fine mesh, a 2D Lagrangian interpolation is used. The algorithm guarantees a smooth variation of physical quantities, which would be adequate only when waves (or discontinuities) do not locate on the fine-coarse mesh boundary. In other words, the refinement criteria must ensure that the waves dwell in the finest mesh and do not travel beyond the fine-coarse mesh boundary during one timestep. In IMPACT, this requirement is achieved through adding a buffer layer to the second derivative-based refinement criteria discussed below.

## 4.3 Refinement criteria

The refinement criteria are critical in mesh refinement since they determine the eventual grid structure in the simulation. In the context of multi-medium compressible flows, higher resolutions are needed where discontinuities of physical quantities are present, such as shocks and interfaces. In IMPACT, we choose the second derivative of density as the conditioned variable for applying the refinement criterion. The pressure and velocity are not selected since they are smooth across contact discontinuities in single-medium

compressible flows. Specifically, the Löhner's estimator for the second derivative is used [49], where the refinement criteria  $c_{refine}$  is written as,

$$c_{refine} = \left\{ \frac{\sum_{pq} \left( \frac{\partial^2 u}{\partial x_p \partial x_q} \right)^2}{\sum_{pq} \left[ \frac{1}{2\Delta x_p} \left( \left| \frac{\partial u}{\partial x_p} \right|_{i_{q+1}} + \left| \frac{\partial u}{\partial x_p} \right|_{i_{q-1}} \right) + \epsilon \frac{|u_{pq}|}{\Delta x_p \Delta x_q} \right]^2} \right\}^{1/2}. \quad (4.2)$$

In the above equation,  $p, q$  represent the horizontal and vertical axis directions respectively, while a small disturbance  $\epsilon = 0.01$  is added to avoid division by zero. The estimator is the normalized second-order central finite difference approximation of the second derivative of the variable considered for refinement. Unless otherwise mentioned, the refinement threshold employed in this work was 0.1, while a de-refinement threshold of 0.02 was used.

For the second refinement criterion, all cells within the computational band of the zero level set ( $\pm 6\Delta dx$  in IMPACT) were tagged for refinement. The two-criteria refinement has been successfully applied in the simulation of multi-material flows [10]. There are two reasons for adding such a criterion. First, as a fourth-order scheme is used for reinitialization and calculating the normal directions, applying the second order prolongation scheme described in Section 4.2, will result in a loss of the higher order of accuracy, thereby affecting the extrapolation and interfacial Riemann problem in R-GFM approach. Secondly, the first refinement criterion solely captures regions with highly discontinuous density profiles, so that only the cells adjacent to the interface will be tagged for refinement. Moreover, as pointed out in [36], de-refining a cell previously occupied by the interface will likely result in instabilities due to the generation of negative pressure. To

address this issue, the authors of [36] suggested using the Natural Neighbor Interpolation (NNI) in place of the regular restriction operator at the interface. Alternatively, leaving a band of cells residing in the finest mesh can circumvent the issue as well, and is the approach used in IMPACT.

The logic diagram for the implementation of the two-criteria refinement in IMPACT is shown in FIGURE 4.2. A block that satisfies either criterion for refinement will be tagged for refinement. On the other hand, a block is de-refined only if it meets both de-refinement criteria.

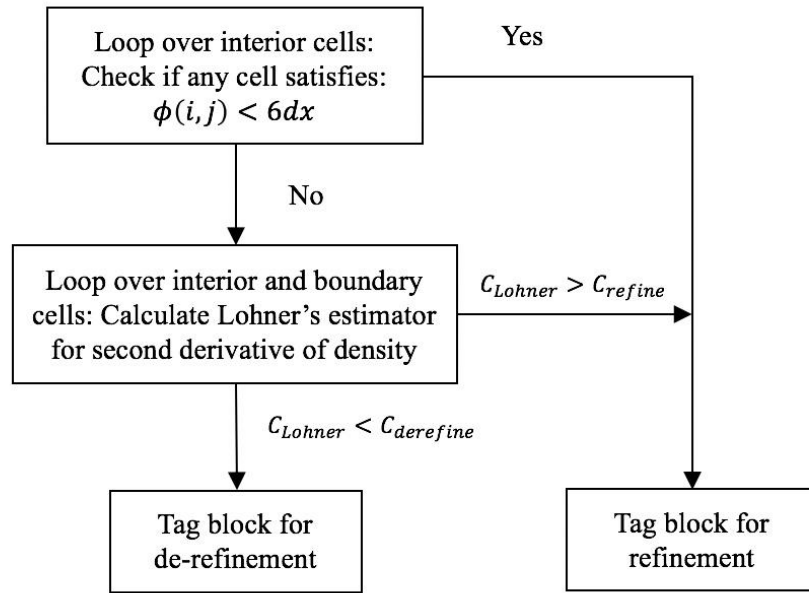


**FIGURE 4.2: Logic flowchart for two-criteria mesh refinement.**

In rare instances, it is possible that a block meets the refinement criterion while all of its child blocks meet the de-refinement criterion. This will result in the block being refined and de-refined repeatedly at every time step, adding to the computational overhead. PARAMESH avoids such difficulties by applying the same refinement criteria to both the

finest blocks and their parents, while making prioritizing the refinement over the de-refinement: e.g. FIGURE 4.3 shows a simple 1D hierarchical block structure ( $2 \times 1$ ). The numbers in red represent the density in each cell, while the density inside the parent block is calculated according to equation (4.1). If the central finite difference scheme is used to approximate the first derivative of density, the right cell inside Parent 1 will meet the refinement criteria whereas the blocks Child 1 and Child 2 will meet the de-refinement criteria. Under such circumstances, Child 1 and Child 2 will not be de-refined in PARAMESH. As a result, an extra restriction operator is always needed to acquire the quantity of interest on the parental blocks, before applying the refinement criteria.

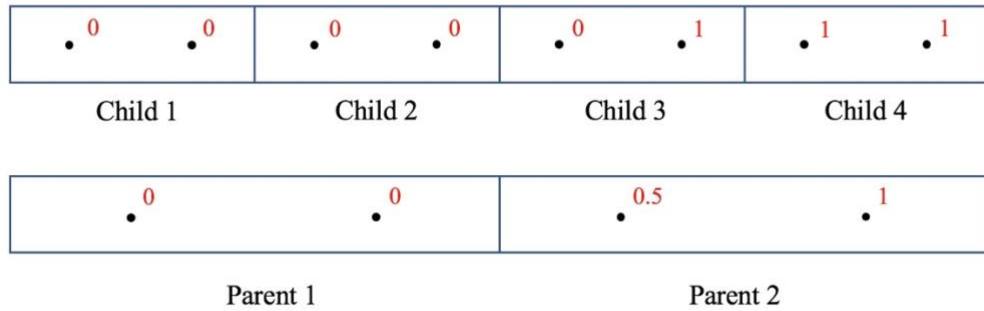


**FIGURE 4.3: An example of recursive mesh refinement.**

#### 4.4 An example on grid structure

In this section, a simple test problem used to verify the effectiveness of the AMR implementation in IMPACT is described. The initial conditions of the physical problem are given in detail in Section 5.2.2. A total of five levels of mesh refinement were used for the problem, with a finest grid spacing of  $1/1024$ . FIGURE 4.4 shows the adaptive mesh overlaid on the numerical Schlieren image. Regions containing the multimedium interface and the transmitted wave in both water and air are refined to the finest levels validating the

choice of refinement criteria employed. To quantitatively describe the efficiency of the adaptive mesh, the percentage Occupancy Ratio is used [10]. The OR is defined as the ratio of the number of cells used in an AMR simulation at a specific time step to the number of cells used in a uniform mesh corresponding to the finest mesh in the AMR simulation:

$$OR = \frac{[N_{cells}(t)]_{AMR}}{(N_{cells})_{finest}}. \quad (4.3)$$

For the numerical test above, the number of blocks at the time of plotting was approximately 11,000, and the resulting OR is 16.7%, which indicates a significant reduction on the computational cost.

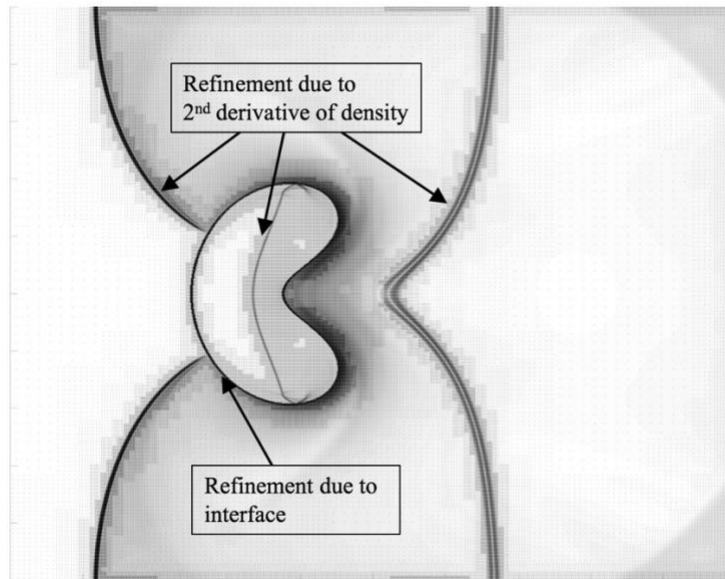


**FIGURE 4.4: Grid structure showing adaptive mesh refinement for a 2D gas-water shock interaction problem.**

## CHAPTER 5: NUMERICAL EXAMPLES

In this chapter, we report on several numerical test cases that serve to validate the improvements made to IMPACT. The focus of 1D test cases is to demonstrate quantitatively, the improved performance of the modified R-GFM when compared with the original R-GFM [17]. The 2D tests involve a wider range of comparisons, and serve to evaluate the relative performances of (i) second-order reinitialization vs. HJ-WENO reinitialization, and the (ii) modified R-GFM vs. the original R-GFM [17]. Collectively, these test cases will show the combination of modified R-GFM and second-order reinitialization produces the most accurate results, characterized in terms of the quality of material interfaces, wave locations and global fidelity to mass conservation.

### 5.1 1D Shock tube problems

#### 5.1.1 Gas-gas shock interactions

**Weak shock interactions:** A 1D shock tube with unit length is considered, and includes air (left) and helium (right) sections separated by a diaphragm in the middle. The dimensionless initial conditions, taken from [17], are given as follows:

$$(\rho, u, P, \gamma) = \begin{cases} (1.0, 0.0, 1.0, 1.4), & \text{for } x \leq 0.5, \\ (0.125, 0.0, 0.1, 1.667), & \text{for } x > 0.5. \end{cases} \quad (5.1)$$

The simulation was performed with AMR and three levels of mesh refinement, where the mesh density at the highest refinement level was  $dx = 1/512$ . The WENO-5/Roe scheme was chosen as the single-phase Riemann solver. The density and pressure profiles at  $t = 0.16$ , are shown in FIGURE 5.1. There is no visible differences in the interface locations between the modified R-GFM and the analytical solutions. However, the location

of the transmitted shock is slightly overpredicted by both the R-GFM and to a lesser extent by the modified R-GFM, according to the magnified plots shown in FIGUREs 5.1(b) and (d). Furthermore, the over-heating error observed at the interface is slightly reduced with the modified R-GFM.

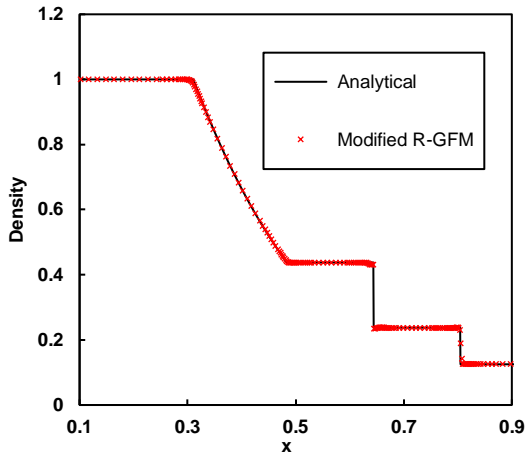
**Strong shock interactions:** The ability of IMPACT to handle strong shock interactions is examined here. The initial conditions for this case are from [50], where the dimensionless initial values for left/right states are:

$$(\rho, u, P, \gamma) = \begin{cases} (1.0, 0.0, 500, 1.6), & \text{for } x \leq 0.5, \\ (1.0, 0.0, 0.2, 1.4), & \text{for } x > 0.5. \end{cases} \quad (5.2)$$

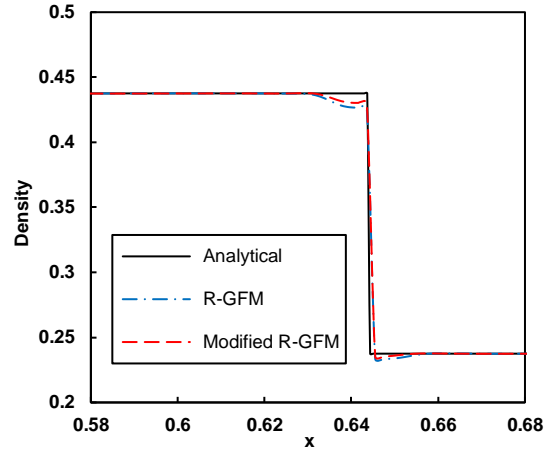
The pressure ratio of left/right state was 2500:1, corresponding to a Mach 31 transmitted shock travelling to the right. Numerical results at  $t = 0.01$  are shown in FIGURE 5.2. Similar to the previous case, the modified R-GFM proposed in this work demonstrates improved performance in capturing the transmitted shock and reducing the overheating errors. The improvement is more evident here than in the previous weak-shock case. Furthermore, when compared with numerical schemes reported elsewhere [36, 51, 52], we find our GFM approach generates fewer oscillations in pressure near the rarefaction wave. Although more accurate GFM schemes have been reported with improved performance in handling overheating errors for 1D (e.g. I-GFM [8]), we emphasize the strength of our approach lies in the enhanced quality of the interface in 2D flows.

The comparison of density profiles between the uniform and AMR meshes is shown in FIGUREs 5.1 (e) and 5.2 (e) for the weak and strong shock interactions respectively. In both cases, the results are in agreement, while regions containing sharp gradients in density and pressure are refined to the finest level. The occupancy ratios for the weak/strong shock

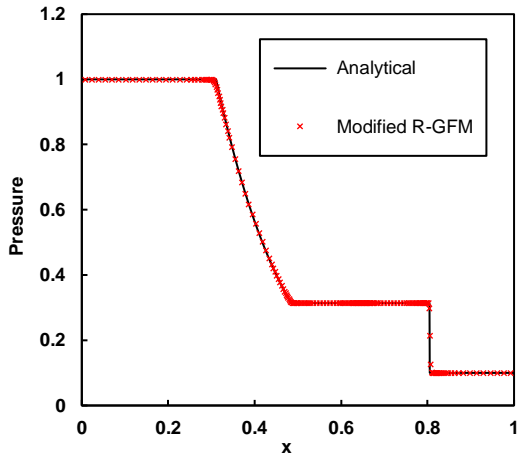
problems at the end of the simulations were 36.7% / 31.4%, indicating significant savings in computational costs.



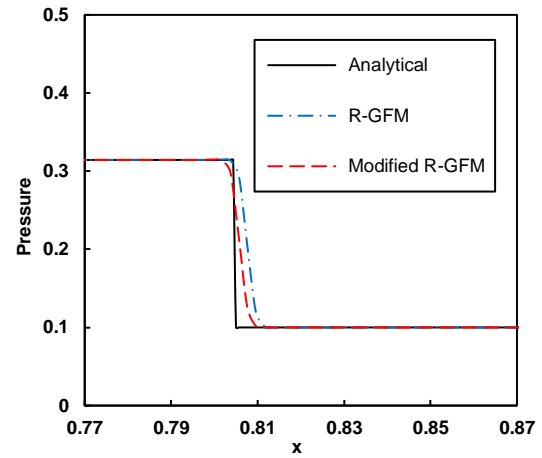
(a)



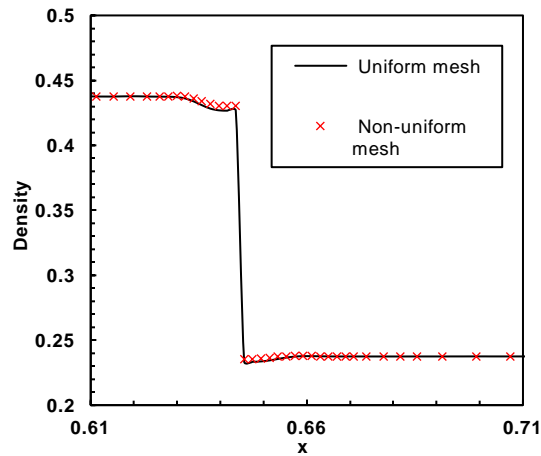
(b)



(c)

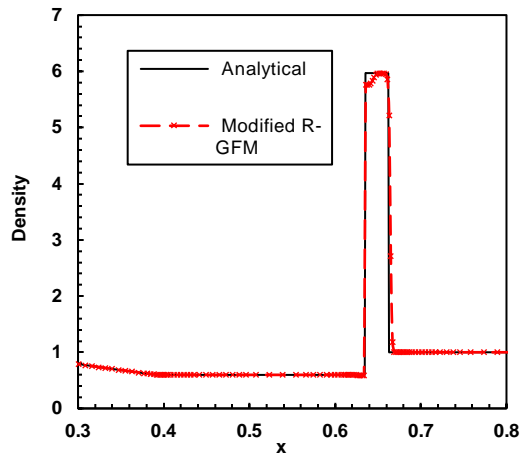


(d)

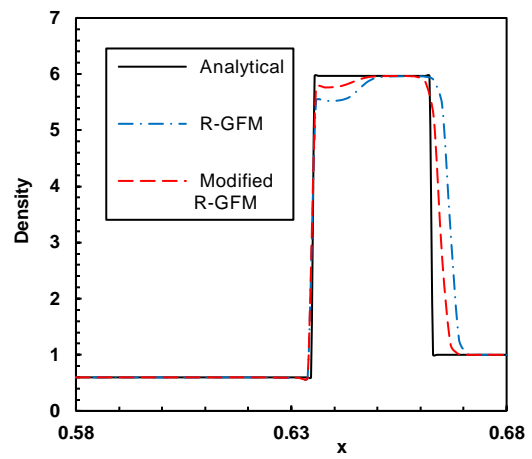


(e)

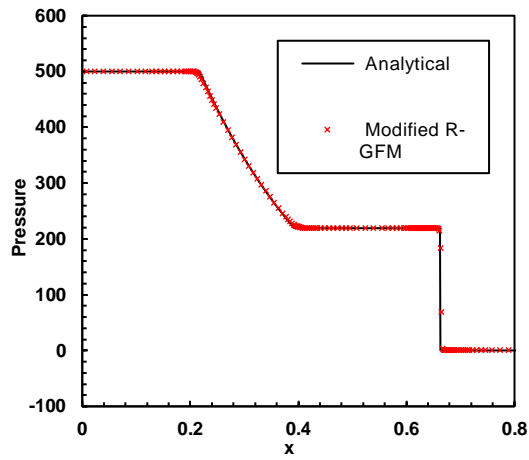
**FIGURE 5.1: Numerical solutions for 1D air-helium shock interactions at  $t = 0.16$ .**



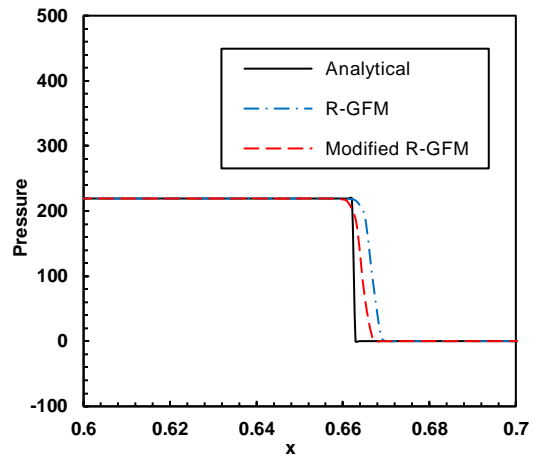
(a)



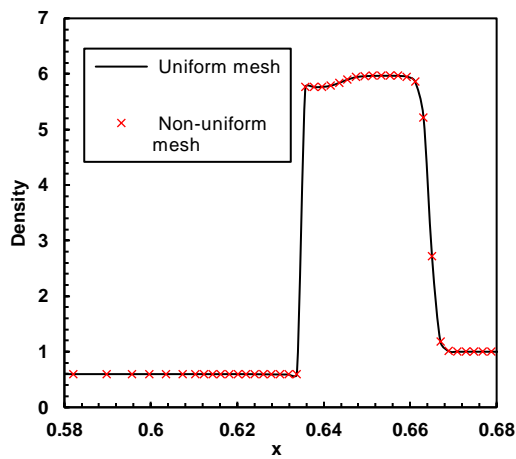
(b)



(c)



(d)



(e)

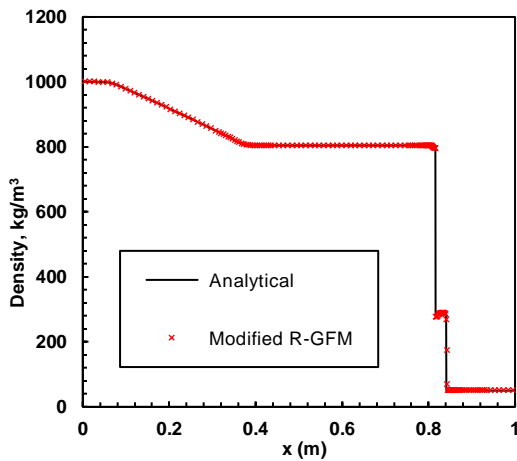
**FIGURE 5.2: Numerical solutions for 1D air-helium strong shock interactions at  $t = 0.01$ .**

### 5.1.2 Gas-water shock interactions

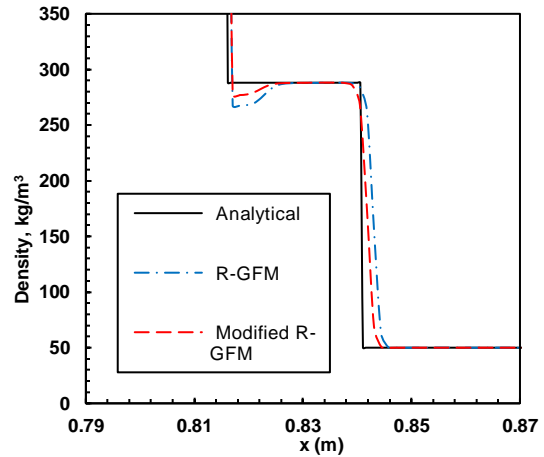
The 1D gas–water shock interaction discussed here involved a large density jump at the material interface, while the stiffened gas equation was used to determine the pressure in water. The initial conditions for the problem were from [53], and written as:

$$\begin{aligned}
 & (\rho, u, P, \gamma, p_\infty) \\
 & = \begin{cases} (1000\text{kg/m}^3, 0\text{m/s}, 10^9 \text{ Pa}, 4.4, 6.0 \times 10^8 \text{ Pa}), & \text{for } x \leq 0.7\text{m}, \\ (50\text{kg/m}^3, 0 \text{ m/s}, 10^5 \text{ Pa}, 1.4, 0 \text{ Pa}), & \text{for } x > 0.7\text{m}. \end{cases} \quad (5.3)
 \end{aligned}$$

The finest mesh used for this simulation was  $dx = 1/768$ . Density and pressure profiles at  $t = 0.24 \text{ ms}$  are shown in FIGURE 5.3 and demonstrate excellent agreement between the modified R-GFM and the exact solution. In addition, the modified R-GFM predicts the locations of the interface and shock more accurately than the original R-GFM.



(a)



(b)

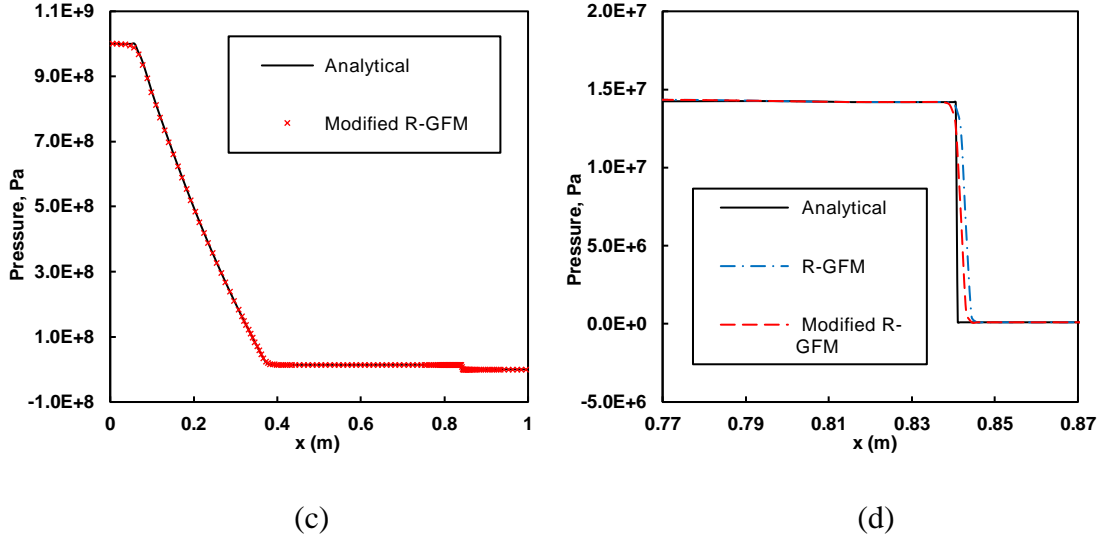


**FIGURE 5.3: Numerical solutions for 1D air-water shock interactions at  $t = 0.24$  ms.**

## 5.2 2D Shock bubble cases

### 5.2.1 Mach 1.22 air–helium shock bubble interaction

Results from the canonical 2D air–helium shock bubble interaction problem are presented in this section. The problem definition is based on the experiments of Hass and Sturtevant [54], which were later used as a benchmark case in several numerical papers [55, 56, 17, 23, 57]. Consider a stationary cylindrical helium bubble placed at the center of a rectangular box in quiescent air. The configuration of the 2D computational domain is demonstrated in FIGURE 5.4, with the geometric parameters defined as follows:

$$a = 44.5 \text{ mm}, \quad b = 356 \text{ mm}, \quad c = 50 \text{ mm}, \quad d = 150 \text{ mm}, \quad e = 25 \text{ mm}$$

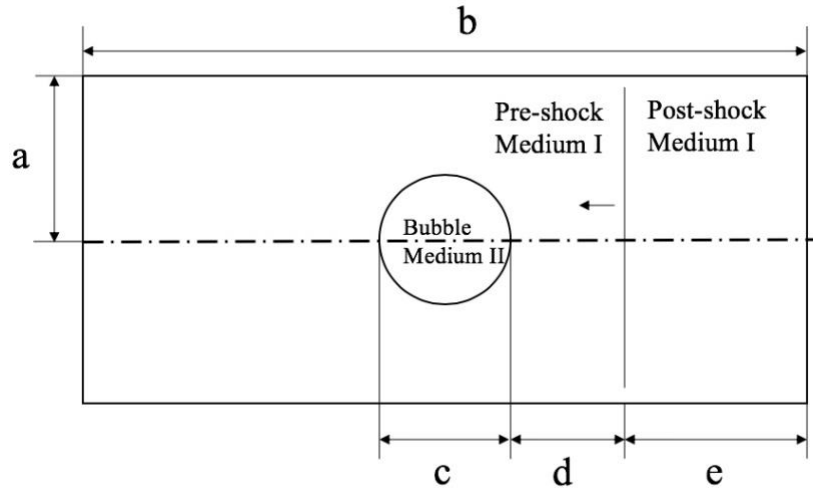


**FIGURE 5.4: Problem setup for the shock bubble problem.**

The initial states for the helium bubble and the surrounding air are:

$$(\rho, u, p, \gamma) = \left\{ \begin{array}{l} 1.78 \text{ kg/m}^3, -110.63 \text{ m/s}, 159060 \text{ Pa}, 1.4, \text{ for post - shocked air} \\ 1.29 \text{ kg/m}^3, 0.0 \text{ m/s}, 101325 \text{ Pa}, 1.4, \text{ for pre - shocked air} \\ 0.235 \text{ kg/m}^3, 0.0 \text{ m/s}, 101325 \text{ Pa}, 1.648, \text{ for helium bubble} \end{array} \right. \quad (5.4)$$

The top/bottom boundaries were treated as periodic, while the left/right boundary surfaces were treated as zero-gradient surfaces. A total of four levels of adaptive mesh refinement were used, corresponding to a finest mesh size of 216 Points Per bubble Radius (p.p.r.). The refinement thresholds for the case were set to:  $c_{refine} = 0.1, c_{derefine} = 0.02$ , while the CFL parameter was chosen to be 0.4.

The numerical Schlieren images of the density gradients associated with the helium bubble at different times are shown in TABLE 5.1, where a comparison between the modified R-GFM with other numerical methods [57] is included. In the figures in TABLE

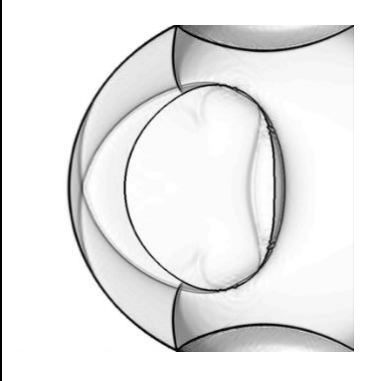
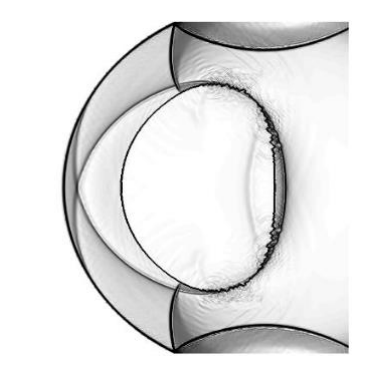
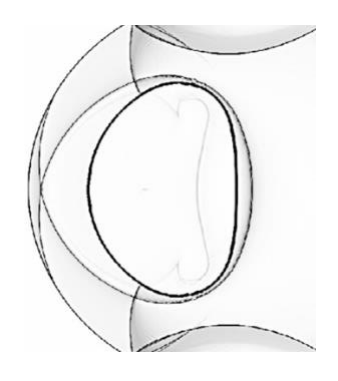
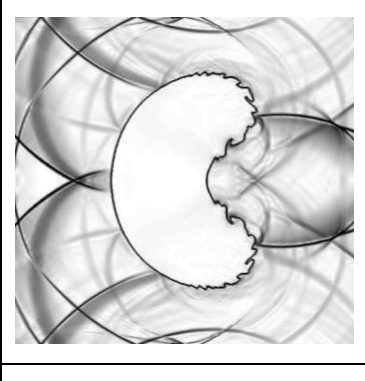
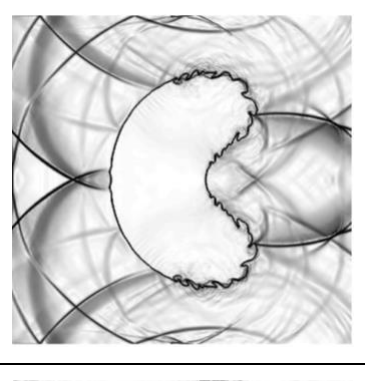
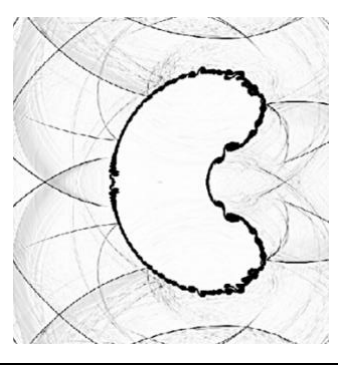
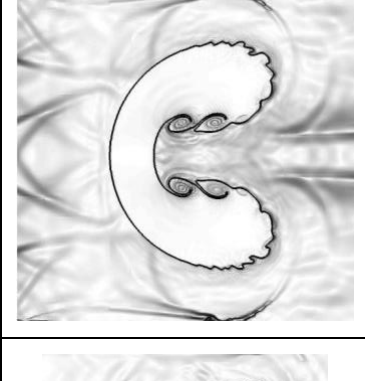
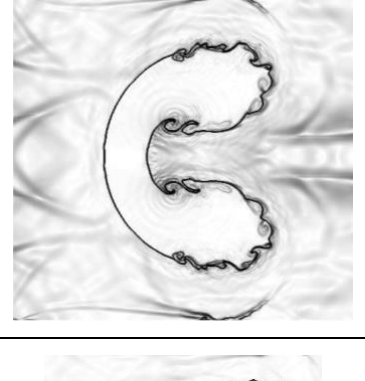
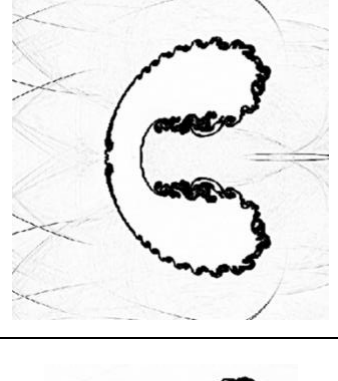
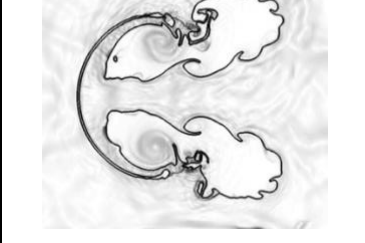
5.1, the instance of shock impingement on the bubble is taken as  $t = 0 \mu s$ . Note that the finest mesh used in the study reported in [57] was 500 p.p.r. As shown in the plots, the locations of the transmitted and reflected waves are in good agreement with results from [57]. During the early stages of the simulation, oscillations in the density field are observed near the top and bottom of the helium bubble when computed using the original R-GFM. In contrast, significant attenuation of these oscillations is observed when the modified R-GFM is instead employed. Also, Richtmyer-Meshkov (RM) [58] and Kelvin-Helmholtz (KH) [59] instabilities can be clearly observed with the modified R-GFM at  $t = 427 \mu s$ ,  $983 \mu s$ , due to the sufficiently large mesh size and the higher fidelity of the method. Even at slightly lower grid resolutions (108 p.p.r. vs. 112 p.p.r. in [17]), the modified R-GFM is capable of revealing more details associated with the interfacial instabilities, as shown in FIGURE 5.6 (a).

FIGURE 5.5 is a plot of the time evolution of the locations of three distinct features of the helium bubble: the downstream, upstream and jet locations. Overall, the results from IMPACT are in good agreement with other numerical approaches [22, 23, 18]. The data from the original R-GFM and the modified R-GFM are in agreement initially, while the deformed bubble computed by the original R-GFM moves slightly faster at late times (the difference in the positions of the interface near the end of the simulation is around 2%). The time-averaged velocity of the upstream interface (144.4 m/s), the downstream interface (174.9 m/s) and the jet (220.1 m/s) from the modified R-GFM were all found to agree with the data from the experiments of [54] within the experimental uncertainty (the velocities of different bubble locations were obtained in the same manner as described in TABLE 2 from [57]).

### **Comparison between second-order reinitialization and HJ-WENO reinitialization**

**schemes:** A comparative study between the different reinitialization schemes was also carried out, and the resulting bubble contours at  $t = 427 \mu s, 674 \mu s, 983 \mu s$  are shown in FIGURE 5.6. We find the choice of reinitialization scheme does not affect the wave locations as the shock propagates through the bubble. However, interfacial instabilities appear more dominant when the second-order reinitialization is used, due to the fact that the interface is fixed through a quadratic interpolation. Such a phenomenon is consistent with the numerical tests reported in Section 2.3.2, where the second-order reinitialization scheme was capable of preserving greater details of the interfacial structures at the same resolution as the HJ-WENO reinitialization. Furthermore, the second-order scheme also demonstrates improved symmetry compared with the HJ-WENO reinitialization, particularly during the early stages of the simulation.

**TABLE 5.1: Numerical Schlieren images of the density gradient for the air-helium shock bubble interaction simulation and comparison with results from [57].**

Time	Modified R-GFM, IMPACT, 216 p.p.r.	R-GFM, IMPACT, 216 p.p.r.	Coralic [57], 500 p.p.r.
102 $\mu s$			
245 $\mu s$			
427 $\mu s$			
983 $\mu s$			

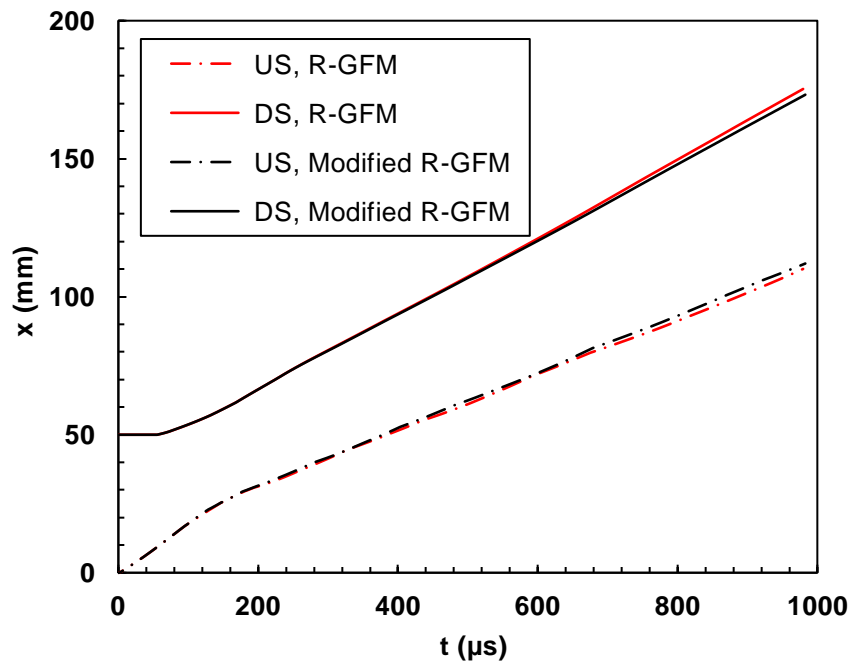
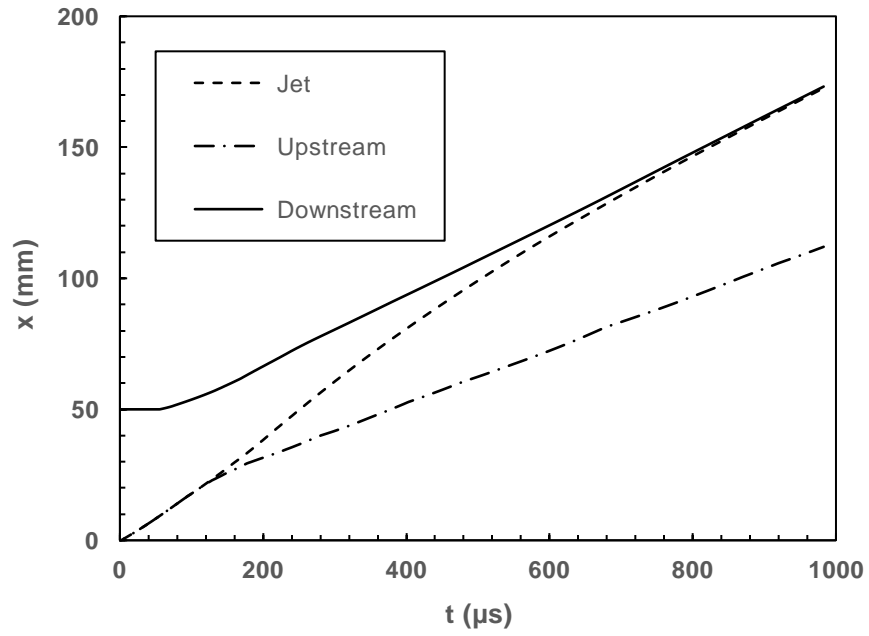
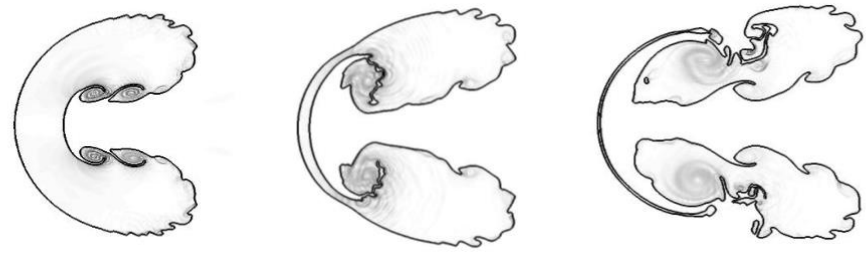


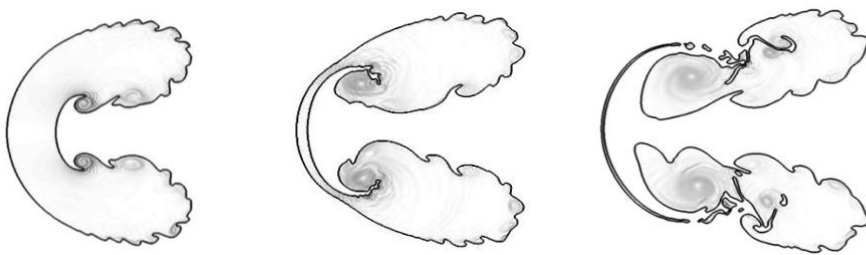
**FIGURE 5.5: Time evolution of downstream, upstream and jet locations for Air-Helium shock bubble problem.**



(a)



(b)



(c)

**FIGURE 5.6: Numerical Schlieren images showing the time evolution of the air-helium shock bubble problem. Left panel: 427  $\mu$ s, Middle panel: 674  $\mu$ s, Right panel: 983  $\mu$ s. (a) Second-order reinitialization (108 p.p.r.) (b) Second-order reinitialization (216 p.p.r.) (c) HJ-WENO reinitialization (216 p.p.r.).**

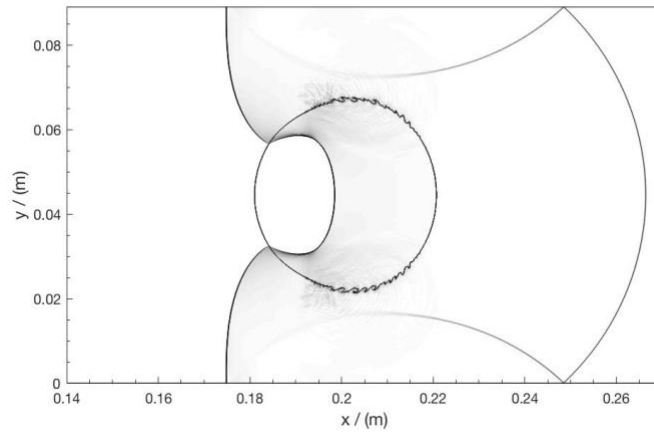
### 5.2.2 Air-R22 shock bubble interaction

Results from IMPACT simulation of an air-R22 shock-bubble interaction problem are presented in this section. The setup of the computational domain is identical to the air-helium problem discussed earlier (FIGURE 5.4), while the initial states of the R22 bubble and the surrounding air are specified as follows:

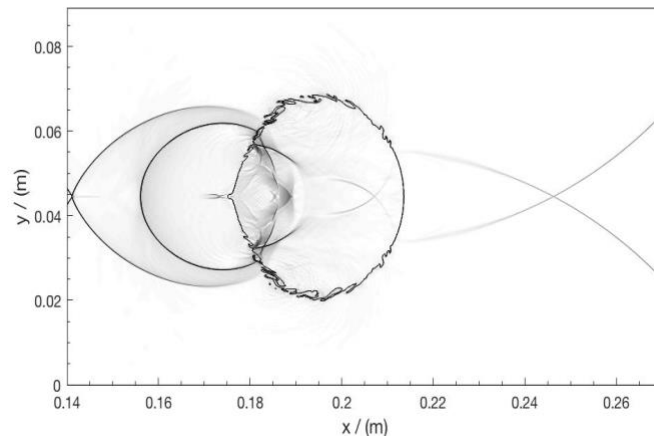
$$(\rho, u, p, \gamma) = \begin{cases} 1.66 \text{ kg/m}^3, -114 \text{ m/s}, 159080 \text{ Pa}, 1.4, & \text{for post - shocked air} \\ 1.2062 \text{ kg/m}^3, 0.0 \text{ m/s}, 101325 \text{ Pa}, 1.4, & \text{for pre - shocked air} \\ 3.5965 \frac{\text{kg}}{\text{m}^3}, \frac{0.0 \text{ m}}{\text{s}}, 101325 \text{ Pa}, 1.1847, & \text{for R22 bubble.} \end{cases} \quad (5.5)$$

The finest mesh used for this case was 432 p.p.r. (corresponding to 1536 cells along the y-direction). An adaptive time step was chosen to satisfy  $CFL = 0.4$ .

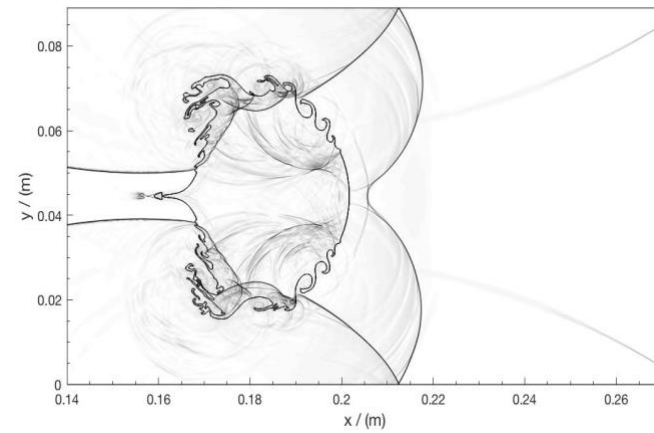
The time evolution of the density gradient contours are shown in FIGURE 5.7. The locations and shapes of the air-R22 interface and the acoustic waves are in good agreement with both experimental [54] and numerical results [52, 60]. A step-by-step description of the mechanism of air-R22 shock bubble deformation was provided in [60]. Since the speed of sound is higher in the R22 bubble, the incident shock speed in air is faster than that of the refracted shock in R-22. Such differences in velocity on the multi-material interface results in the counter-clockwise (clockwise) KH instability observed on the upper(lower)-half of the R22 interface. Due to the high resolution employed here, the RM and KH instabilities are clearly observed with the modified R-GFM. Compared with the numerical results from the original R-GFM presented in [19], the modified R-GFM captures more structures while generating fewer oscillations in density at the same resolution.



**(a) 135  $\mu s$**



**(b) 247  $\mu s$**



**(c) 417  $\mu s$**

**FIGURE 5.7: Numerical Schlieren images of shock-induced R22 bubble collapse in air.**

### 5.2.3 Mach 1.43 water-air shock-bubble interaction:

In this test problem, a Mach 1.43 shock originating in water impinges on an air bubble and serves to verify the ability of IMPACT in simulating multiphase compressible flows. The Weber number is calculated based on the maximum jet speed behind the air bubble and the width of the water jet [61]. For this problem in particular, the Weber number exceeds  $10^3$  [62, 61], therefore surface tension forces do not play a significant role. The computational domain is parametrized similar to the previous case (FIGURE 5.4), with the following geometric parameters defining the locations of the bubble and the shock:

$$a = 1 \text{ mm}, b = 2 \text{ mm}, c = 1 \text{ mm}, d = 0.1 \text{ mm}, e = 0.4 \text{ mm} .$$

To minimize boundary effects on wave structures and interfaces, all boundary conditions in the problem were set to zero gradient conditions. The initial conditions used are detailed below:

$$(\rho, u, p, \gamma) = \begin{cases} 1233.4 \text{ kg/m}^3, & -439.8 \text{ m/s}, & 1.02 \times 10^9 \text{ Pa}, & \text{for post - shocked water} \\ 1000.0 \text{ kg/m}^3, & 0.0 \text{ m/s}, & 1.0 \times 10^5 \text{ Pa}, & \text{for pre - shocked water} \\ 1.0 \text{ kg/m}^3, & 0.0 \text{ m/s}, & 1.0 \times 10^5 \text{ Pa}, & \text{for air bubble} \end{cases} \quad (5.6)$$

The simulations were performed at mesh resolutions of 256 p.p.r. and 384 p.p.r. (which correspond to  $N_y = 1024$  and  $1536$  respectively), while four levels of refinement were used for both simulations. The refinement thresholds were set as  $c_{refine} = 0.04, c_{derefine} = 0.005$  and the timestep was constrained to satisfy  $CFL = 0.4$ . The single-medium Riemann problem was solved using the WENO-5/Lax-Fredrich scheme.

Schlieren images of the density gradient at different simulation times are shown in FIGURE 5.8. The interface contours are in qualitative agreement with those reported in the literature [39, 63]. However, the locations of the wave structure in the current study are closer to Hawker's [63] results, who used 400 p.p.r combined with a front-tracking scheme. From [63], the wave oscillations can be attributed to the use of component-wise WENO reconstruction. In contrast, even at the slightly lower resolutions employed here, IMACT is capable of accurately capturing the wave and interface structure with fewer oscillations.

A detailed description of the mechanism of 1Gpa air-water shock interaction can be found in [63], and briefly reviewed here in the context of our results. Three phases of bubble evolution can be identified: The transition between phases 1 and 2 appear to be marked by the formation of the water-hammer shock seen in FIGURE 5.8 (c), while phases 2 and 3 are separated by the complete passage of the water hammer shock through the air bubble [FIGURE 5.8 (f)]. The large density ratio between the fluids enhances baroclinic vorticity deposition, but suppresses KH instabilities in accordance with linear theory [64]. As a result, the use of different reinitialization schemes does not significantly impact fine-scale features on the interface. When the transverse water jet breaches the upstream portion of the air bubble, the simulation enters the second stage, where the water-hammer shock is predominant. Two sheet-jets are also formed shortly following the emergence of the water-hammer shock and penetrate through the air bubble. At the start of this second phase, the maximum pressure due to the water-hammer shock reaches  $\sim 3.36 \text{ Gpa}$ . This extremely large pressure ratio and the presence of the sharp interface near the tip of the sheet jet increases the likelihood of negative pressures in both water and air, leading to the simulation using original R-GFM becoming numerically unstable. Quantitative parameters

from the above transition are reported in TABLE 5.2, where the results from IMPACT are compared with the literature [63, 18].

Numerical Schlieren images in FIGURE 5.9 depict in detail the moment the water-hammer shock first forms. Compared with numerical results obtained from [10], our implementation of the R-GFM shows significantly reduced oscillations in the density field behind the water jet. Furthermore, the original R-GFM and the modified R-GFM show good agreement in the shape of the interface and the locations of waves, with the exception of slight density oscillations visible near the irregular refraction wave. These results are also in qualitative agreement with the simulation results from the front tracking scheme in [63]. Note that the original R-GFM transitions to the second stage slightly earlier than the area-averaged R-GFM ( $666\text{ ns}$  vs.  $668\text{ ns}$ ). This slight discrepancy is attributed to the way the interfacial ghost points are defined in each case: in the original R-GFM, the interfacial cells are corrected once a wave enters the region within  $1.5dx$  of the interface, whereas in the modified R-GFM, the correction step is applied to the ghost portion of the interfacial cells only.

The mass conservation error of the air bubble at any time instant,  $T = t$ , is defined as follows:

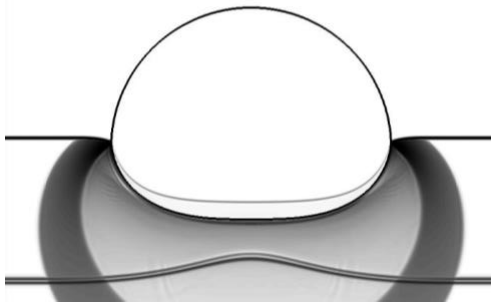
$$Error = \frac{(Mass_{air}|_{T=t} - Mass_{air}|_{T=0})}{Mass_{air}|_{T=0}} \quad (5.7)$$

The evolution of mass conservation errors is shown in FIGURE 5.10 (a) for the modified R-GFM at different mesh resolutions. The error increases dramatically at two instants: (i) the moment when the water hammer shock is formed, and (ii) when the secondary jet first appears. Peaks in the reported mass conservation error at different effective meshes are

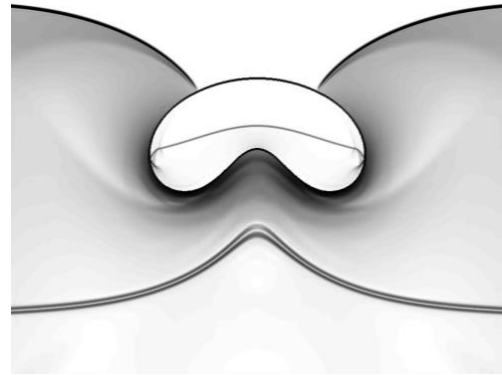
24.2% at 128 p.p.r., 12.7% at 256 p.p.r. and 9.0% at 384 p.p.r. A comparison with the mass conservation error from the original R-GFM [17] is plotted in FIGURE 5.10 (b). For the same resolution, this figure shows the modified R-GFM is able to reduce the conservation error by approximately 50% from the original R-GFM approach. Compared with other sharp interface approaches, such as the Characteristic-Based Method (CBM) of [36], the modified R-GFM reveals larger mass conservation errors during the early stages of the simulation. However, at late times the bubble mass in the modified R-GFM is restored shortly after the formation of the secondary jets, whereas the mass of the bubble continues to increase when computed using the CBM [36].

**TABLE 5.2: Quantitative data during the transition stage of a 1Gpa water-air shock interaction, with comparison with the front tracking method [63] and grid-aligned GFM [18].**

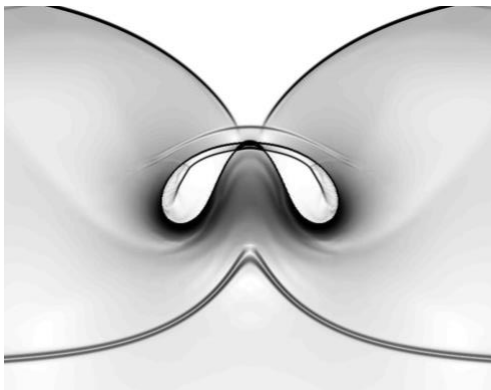
	Modified R-GFM	Hawker [63]	Nikolaos [18]
Resolution (p.p.r.)	256	400	400
First stage time (ns)	668	675	680
Jet speed at impact (m/s)	2111	2278	2131
Water hammer pressure (Gpa)	3.36	3.00	3.48



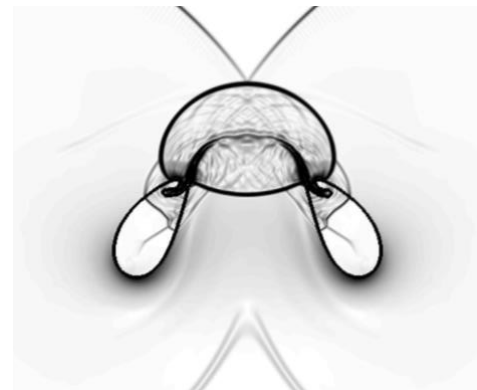
(a) 230 ns : Phase 1



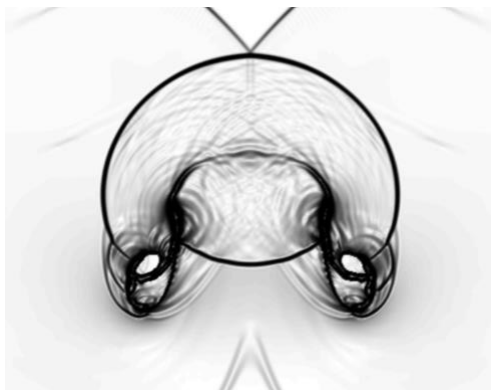
(b) 545 ns : Phase 1



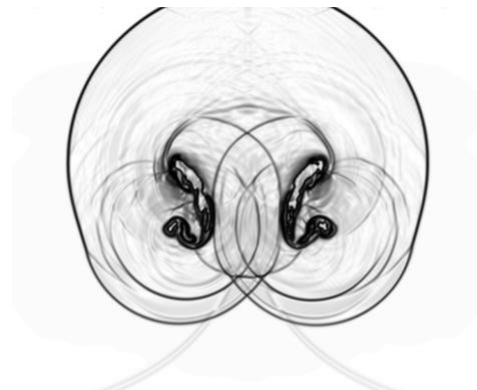
(c) 665 ns : Transition to Phase 2



(d) 725 ns : Phase 2

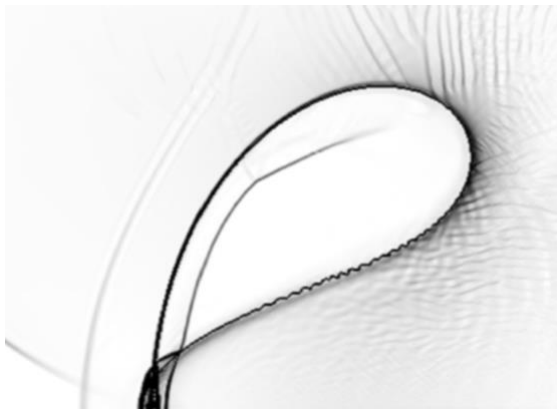


(e) 775 ns : Phase 2

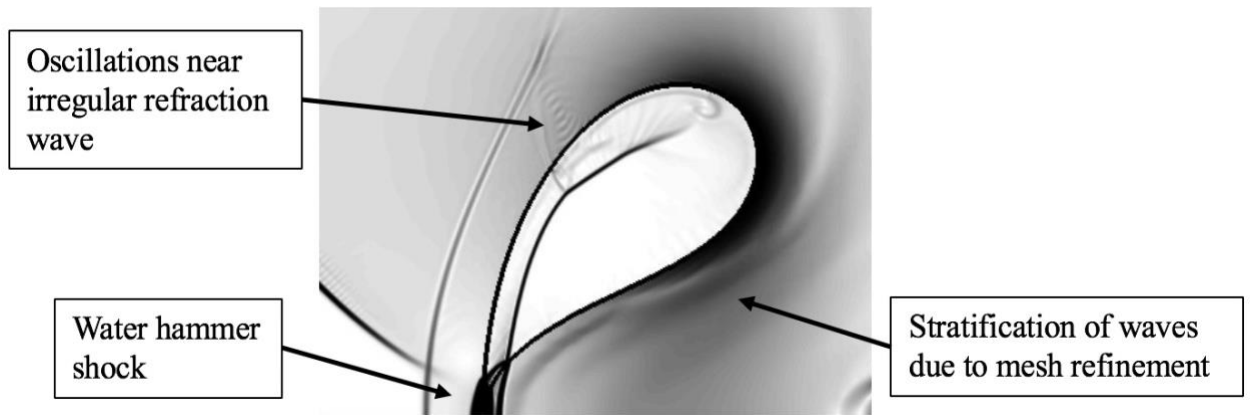


(f) 875 ns : Transition to Phase 3

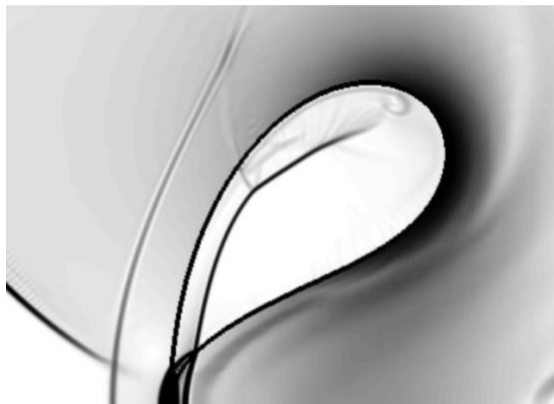
**FIGURE 5.8: Numerical Schlieren images of the interaction between a 1 Gpa water shock and an air bubble.**



(a) Hawker [63], 675 ns, 400 p.p.r.

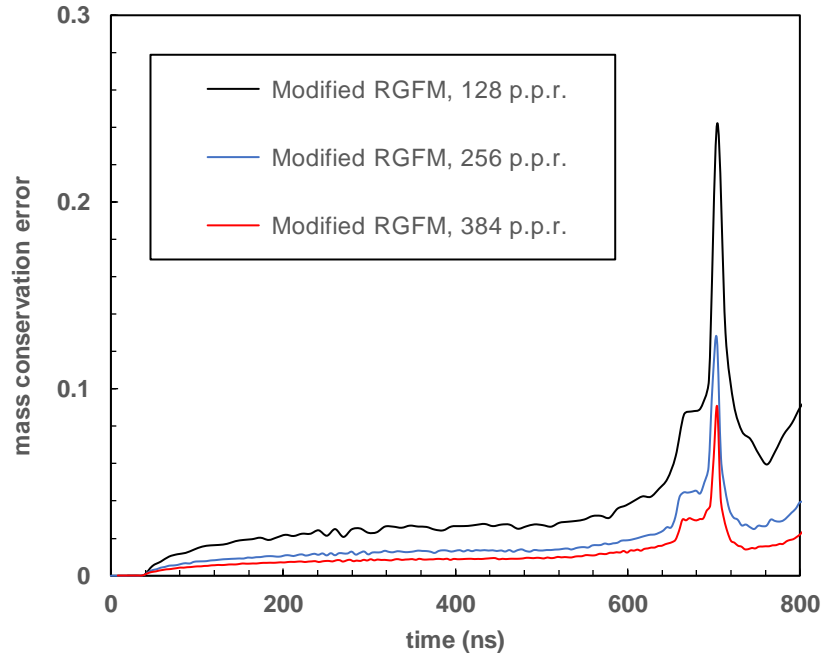


(b) R-GFM IMPACT, 666 ns, 256 p.p.r.

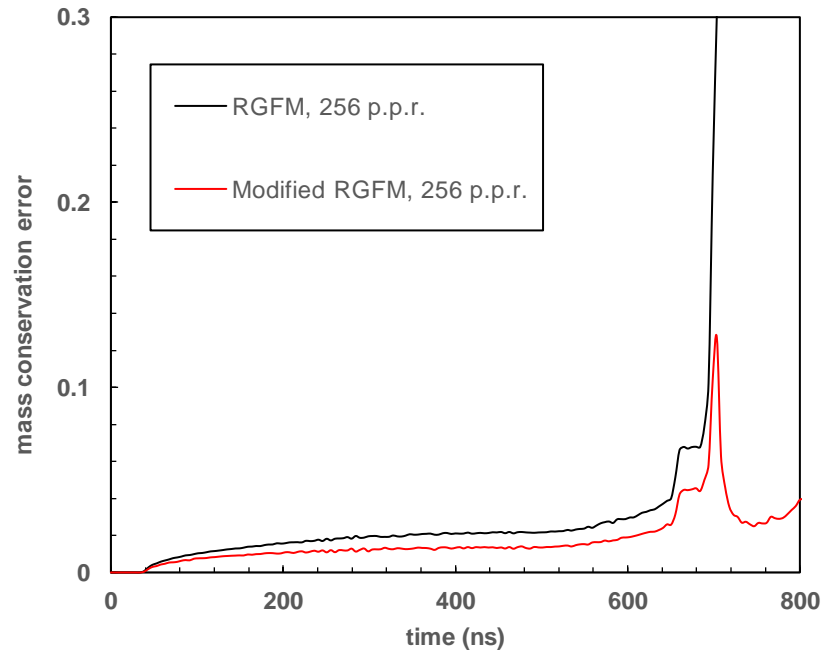


(c) Modified R-GFM IMPACT, 668 ns, 256 p.p.r.

**FIGURE 5.9: Closeup view of density gradient contours when water-hammer shock is formed: Comparison between different numerical schemes.**



(a) Mass conservation error at different mesh sizes.



(b) Comparison with the original R-GFM.

**FIGURE 5.10: Mass conservation errors for the 1.0 Gpa water shock impinging on an air bubble problem.**

### 5.2.4 The Richtmyer-Meshkov instability

The Richtmyer-Meshkov instability (RMI) occurs when two fluids separated by a perturbed interface are impulsively accelerated [58]. In particular, the special case of a planar shock impinging on a sinusoidal material interface separating air and SF<sub>6</sub> is investigated. The computational domain is shown in FIGURE 5.11, with the following geometric parameters:

$$a = 0.5, \quad b = 11, \quad c = 0.35, \quad d = 0.5$$

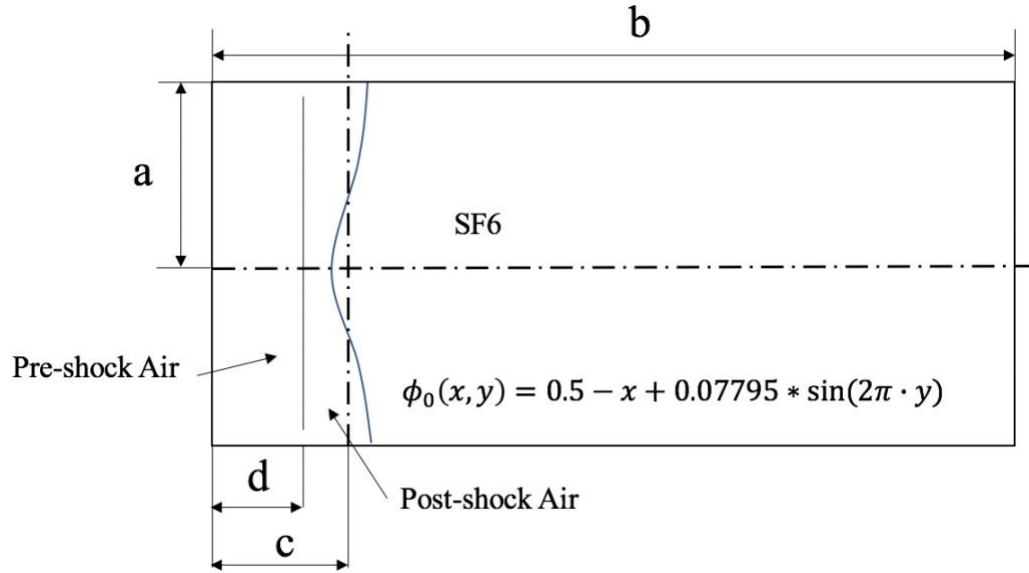


**FIGURE 5.11: The computational domain and geometric parameters for Richtmyer-Meshkov instability simulation (not to scale).**

The initial states for the air and SF<sub>6</sub> streams are

$$(\rho, u, p, \gamma) = \begin{cases} 0.6708 \text{ kg/m}^3, 161.7 \text{ m/s}, 1.513 \times 10^5 \text{ Pa}, 1.4, & \text{for post - shocked air} \\ 0.5 \text{ kg/m}^3, 0.0 \text{ m/s}, 1.0 \times 10^5 \text{ Pa}, 1.4, & \text{for pre - shocked air} \\ 2.5 \text{ kg/m}^3, 0.0 \text{ m/s}, 1.0 \times 10^5 \text{ Pa}, 1.093, & \text{for SF}_6 \end{cases} \quad (5.8)$$

The Atwood number is defined as,

$$A = \frac{(\rho_{SF6} - \rho_{air})}{(\rho_{SF6} + \rho_{air})} \quad (5.9)$$

The corresponding pre-shock Atwood number for this problem was  $A^- = 2/3$ . The WENO-5/Roe solver was used as the single-medium flow solver. The simulation was performed at two levels of the finest mesh:  $\frac{dx}{\lambda} \approx \frac{1}{256}, \frac{1}{512}$ , while the coarsest mesh was fixed at  $\frac{dx}{\lambda} \approx \frac{1}{64}$ , where  $\lambda = 1m$  is the perturbation wavelength. The time step size was adaptively chosen to satisfy  $CFL = 0.5$ . As suggested in [65], the simulation time was non-dimensionalized using,

$$\tau = V_0 \frac{2\pi}{\lambda} t \quad (5.10)$$

where  $V_0 = V_{int} \frac{2\pi}{\lambda} h_0 A^+$  denotes the initial linear growth rate of the interface assuming the flow is largely devoid of compressible effects,  $t$  is the actual simulation time,  $h_0$  is the post-shock amplitude of the interface,  $A^+$  is the post-shock Atwood number and  $V_{int} = 107.6 m/s$  is the velocity of the unperturbed interface (obtained from a companion simulation with  $h_0 = 0$ ).

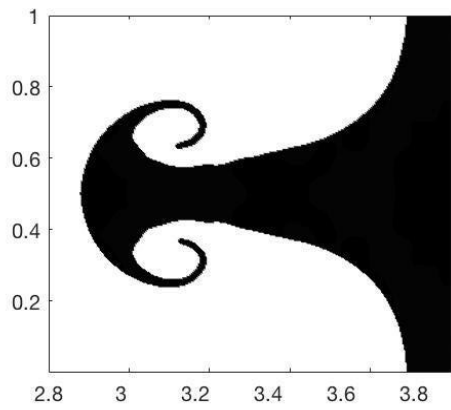
Density profiles at two time instants  $\tau = 5, 10$  are shown in FIGURE 5.12 and for different resolutions. Since the WENO-5 approach is less dissipative at higher resolutions [66], the mushroom structures appear to be more unstable at the higher resolutions (and at late times) and hence fragment. For the same reason, the secondary Kelvin-Helmholtz instability near the mushroom stem is observed only at the finer mesh. A common issue with multimediuim flow solvers is that in the absence of diffusion (e.g. level set/front

tracking method), the shape of the spike will either become too pointed [22] or too flat [36, 10]. Similar shortcomings are also observed in our implementation of the original R-GFM (TABLE 5.3, third row). In contrast, the modified R-GFM does not exhibit such artefacts in the spike shape, which indicates the assignment of the solution from the two-fluid Riemann problem directly to the interfacial cell might be responsible for this behavior.

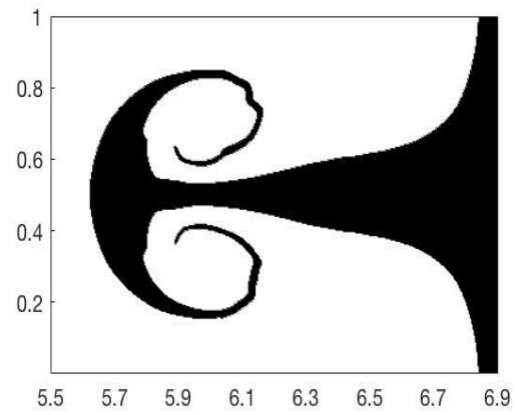
#### 5.2.4.1 Comparison between the different reinitialization schemes

The performances of different reinitialization schemes are compared in TABLE 5.3. In the early stages ( $\tau \leq 3$ ), the interfacial contours from the HJ-WENO reinitialization and the second-order reinitialization are nearly identical. At later times ( $\tau = 5$ ), the second-order reinitialization allows the tip of the mushroom structure to grow further. Additionally, there is no visible difference in the locations of spikes and bubbles, indicating the growth rates of these features are unaffected by the choice of the different reinitialization schemes.

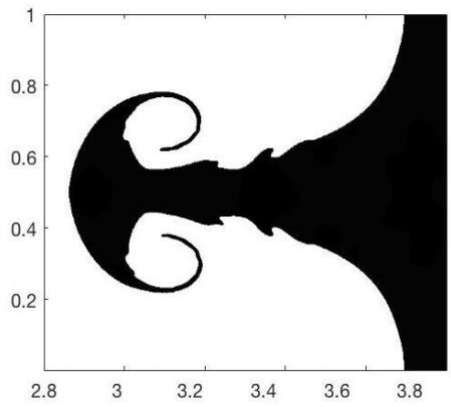
The interfacial contours obtained from the fourth-order reinitialization scheme [30] is shown in FIGURE 5.13 (a) for  $\tau = 5$ . When the fourth-order scheme is used, the tip of the mushroom structure extends further without merging with nearby portions of the interface. If the cubic interpolation to obtain the intersection between the interface and the Cartesian mesh is replaced with a quadratic interpolation [FIGURE 5.13 (b)] as discussed in Section 2.2.1, the interface behavior is similar to the results obtained from the HJ-WENO reinitialization. This suggests the second-order reinitialization is sufficient to capture all details of the interface evolution.



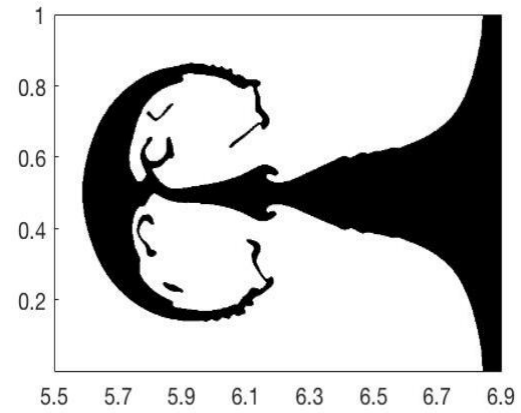
(a)



(b)



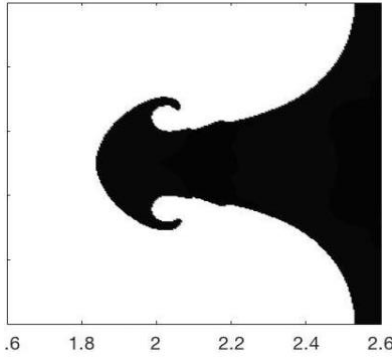
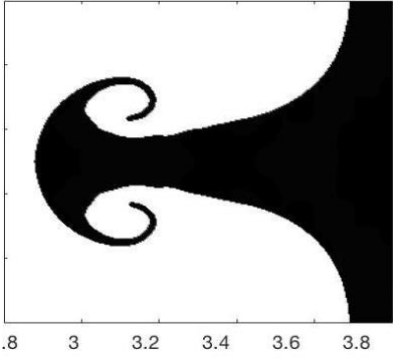
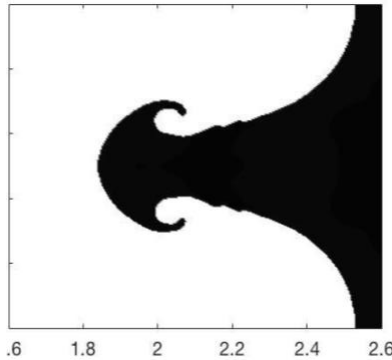
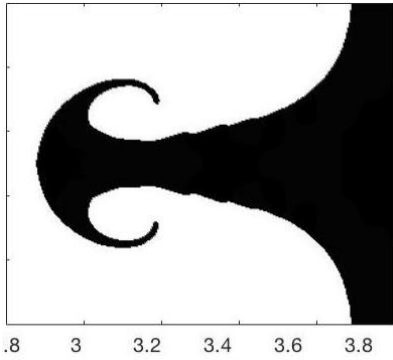
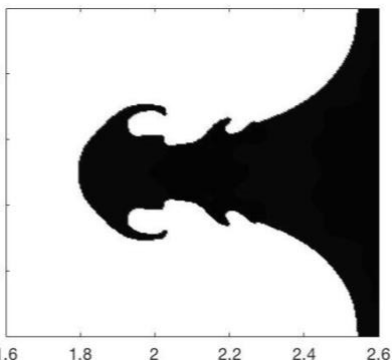
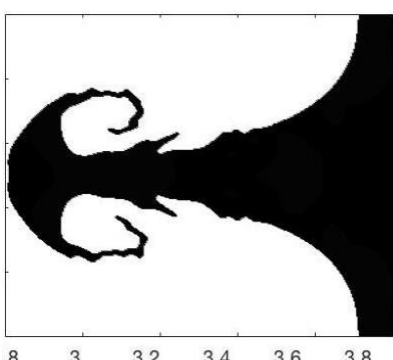
(c)



(d)

**FIGURE 5.12: Density contours from the Air-SF6 RMI simulation at (a)  $\tau=5$ ,  $dx/\lambda=1/256$ , (b)  $\tau=10$ ,  $dx/\lambda=1/256$ , (c)  $\tau=5$ ,  $dx/\lambda=1/512$ , (d)  $\tau=10$ ,  $dx/\lambda=1/512$ .**

**TABLE 5.3 Density contours of the 2D Air-SF6 Richtmyer-Meshkov instability ( $dx/\lambda=1/256$ ).**

Scheme	$\tau = 3$	$\tau = 5$
Modified R-GFM with second-order reinitialization		
Modified R-GFM with HJ-WENO reinitialization		
Original R-GFM with second-order reinitialization		

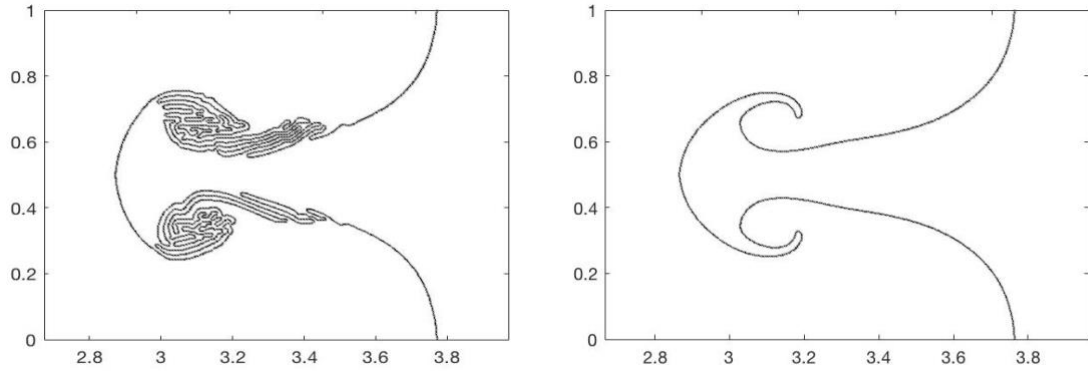


**FIGURE 5.13: Interface contours from the 2D Air-SF6 RMI simulation with fourth-order reinitialization of the level set function ( $dx/\lambda=1/256$ ) and (a) cubic interpolation and (b) quadratic interpolation.**

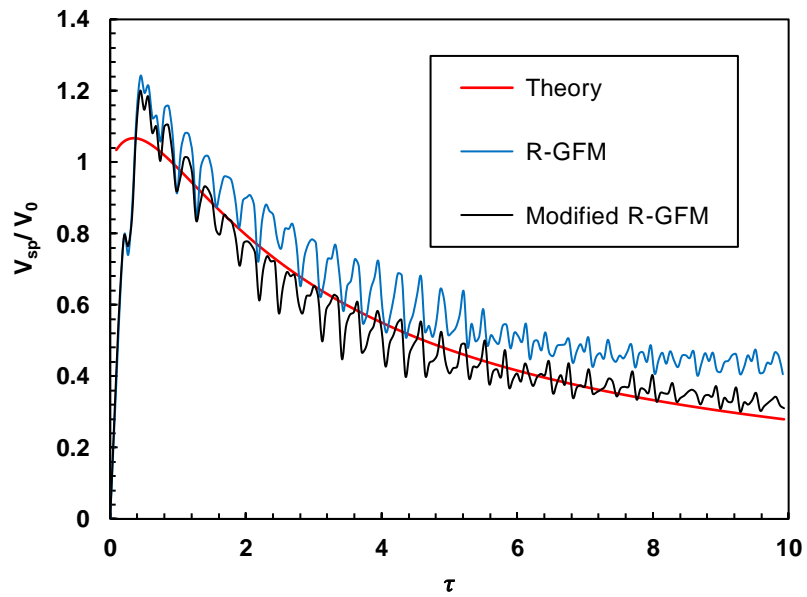
#### 5.2.4.2 RMI growth rates

The growth rate of the RM interfacial perturbation obtained from the numerical simulations is compared with the nonlinear model of Dimonte and Ramaprabhu [65]. The model of [65] has been demonstrated to be valid over a wide range of Atwood numbers and perturbation amplitudes, under the proviso that the flow can be assumed to be incompressible. The spike and bubble growth rates are given by [65],

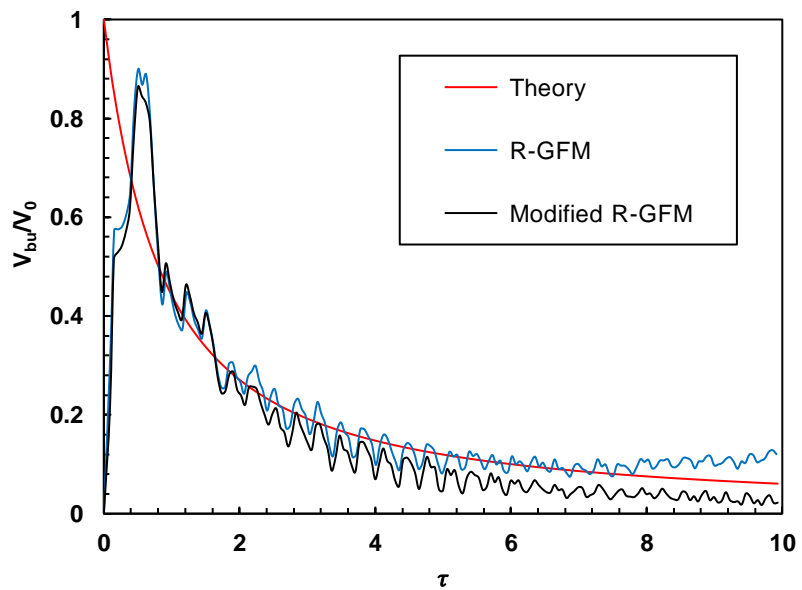
$$V_{bu/sp} = V_0 \frac{1 + (1 \mp |A^+|) \tau}{1 + C_{bu/sp} \tau + (1 \mp |A^+|) (1 \pm |A^+|) \tau^2} \quad (5.11)$$

with  $C_{bu/sp} = V_0 \frac{4.5 \pm |A^+| + (2 \mp |A^+|) |kh_0^+|}{4}$ . The post-shock Atwood number and perturbation amplitudes for this case were  $A^+ = 0.6960$ ,  $kh_0^+ = 0.4159$ . FIGURE 5.14 shows the time evolution of the perturbation growth rates from the original and modified R-GFM approaches, and a comparison with equation (5.11). The mesh size used for both cases was  $\frac{dx}{\lambda} = \frac{1}{512}$ , and was chosen to ensure convergence of key global quantities. From the plots in FIGURE 5.14, the modified R-GFM demonstrates good agreement with equation (5.11)

for the bubble and spike growth rates, whereas the original R-GFM slightly overpredicts the growth rate of the spike. The corresponding growth rates at different mesh resolutions ( $\frac{dy}{\lambda} = \frac{1}{256}, \frac{1}{512}$ ) are shown in FIGURE 5.15. For the mesh resolutions employed here, the RMI bubble and spike growth rates appear to be converged in FIGURE 5.15, with the results at  $\frac{dy}{\lambda} = \frac{1}{512}$  showing slightly fewer oscillations.

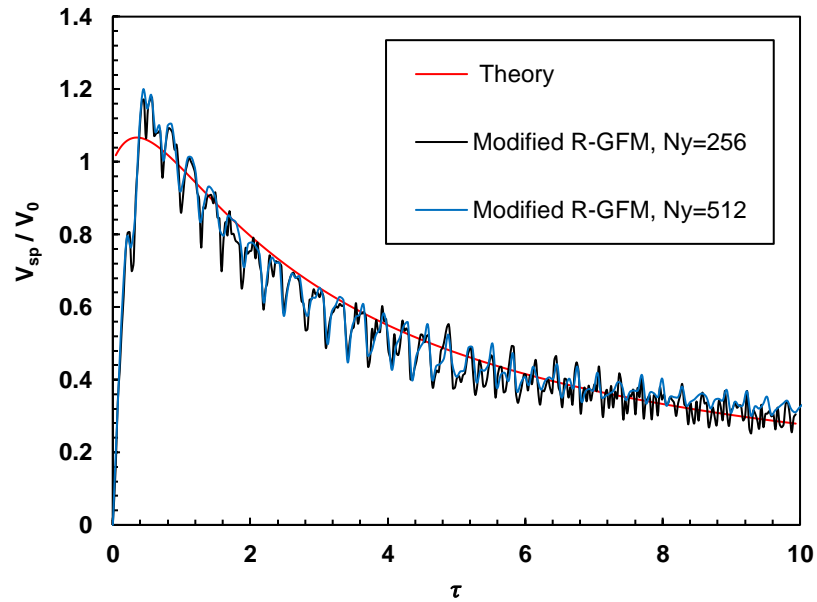


(a)

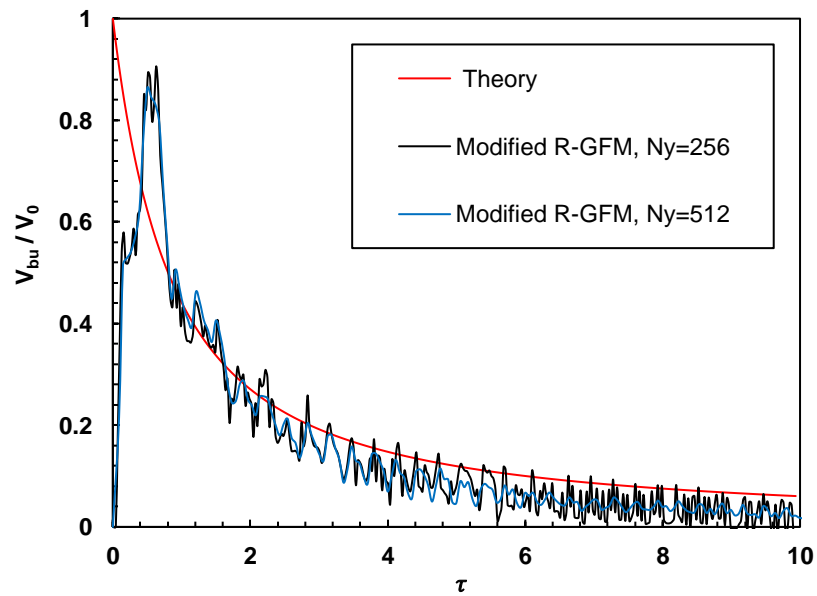


(b)

**FIGURE 5.14: (a) Spike and (b) bubble growth rates from simulations of the Air-SF6 RMI problem using the original and modified versions of R-GFM.**



(a)



(b)

**FIGURE 5.15: (a) Spike and (b) Bubble growth rates from IMPACT simulations using the modified R-GFM approach and showing convergence with respect to the mesh.**

## CHAPTER 6: CONCLUSIONS

A multimediuim compressible flow solver, featuring a modified Riemann-ghost fluid method, the second-order level set approach and block-structured mesh refinement has been presented in this thesis. Preliminary results show the solver is capable of accurately simulating gas-gas and gas-liquid compressible flows with sharp interfaces and complex topology changes. Such problems are relevant to several practical applications in engineering and to naturally occurring flow phenomena.

The central contribution of this work is a modification to the Riemann ghost fluid method (R-GFM [17]) that improves upon the performance of that original approach in resolving interfaces and computing the locations of wave fields generated in such flows. In the proposed scheme, primitive variables on interfacial cells are adjusted based on the area fraction of the ghost/real volumes, determined through a cut-cell approach. Compared with the original R-GFM approach, unphysical oscillations of the interface and the density field are significantly mitigated, as verified through various multimediuim gas-gas compressible flow simulations. In addition, the higher fidelity of the approach is evident as more pronounced growth of interfacial instabilities (KH, RM) for the same resolution as the original R-GFM scheme. Moreover, the modified R-GFM approach demonstrates improved performance in limiting mass conservation errors in simulations of both gas-gas and gas-liquid compressible flows.

Three different reinitialization schemes of the level set method were also evaluated. The second-order reinitialization [13] demonstrates the best performance in predicting the evolution of multimediuim interfaces in terms of robustness and accuracy. The fourth-order reinitialization [30], in spite of its high accuracy, does not accurately predict topology

changes of the interface (such as breakup or merging), when it is applied to solve complex multi-component flow problems. This is attributed to the use of cubic interpolation in acquiring the interface location. A more robust and higher-order scheme should be explored to accurately capture the intersection between the interface and the mesh.

**Future work:**

We identify two directions worthy of further exploration:

1. The modified R-GFM approach achieves improved accuracy by preserving physical quantities in the real portions of interfacial cells. However, the ghost portion of the interfacial cell is still defined through constant extrapolation, which leads to first order of accuracy of the scheme in 2D. To achieve higher orders of accuracy on the interfacial boundary conditions, the primitive variables within the ghost region should be defined through a higher-order extrapolation [67].
2. It was pointed out in [68] that the original R-GFM might fail in handling complex geometries, when the cell used for bilinear interpolation lies in the ghost region. We find that when the modified R-GFM is used in our flow solver to simulate air-water shock interactions at high resolution, the simulation is numerically unstable. To resolve the issue, the authors of [68] suggested using a dynamic probe length in combination with the M-GFM or R-GFM approaches (e.g. in regions with complex geometries, the modified-GFM [16] is used instead of R-GFM). It remains to be seen, if a combination of the cut-cell method suggested here and the hybrid-GFM approach further improves the stability of the numerical solver.

## REFERENCES

- [1] J. YANG, T. KUBOTA and E. E. ZUKOSKI, *Applications of shock-induced mixing to supersonic combustion*, AIAA Journal, 31 (1993), pp. 854-862.
- [2] J.-Y. CHOI, I.-S. JEUNG and Y. YOON, *Computational Fluid Dynamics Algorithms for Unsteady Shock-Induced Combustion, Part 1: Validation*, AIAA Journal, 38 (2000), pp. 1179-1187.
- [3] A. VOGEL, S. BUSCH and U. PARLITZ, *Shock wave emission and cavitation bubble generation by picosecond and nanosecond optical breakdown in water*, The Journal of the Acoustical Society of America, 100 (1996), pp. 148-165.
- [4] M. DELIUS, R. DENK, C. BERDING, H.-G. LIEBICH, M. JORDAN and W. BRENDEL, *Biological effects of shock waves: Cavitation by shock waves in piglet liver*, Ultrasound in Medicine & Biology, 16 (1990), pp. 467-472.
- [5] M. SACKMANN, M. DELIUS, T. SAUERBRUCH, J. HOLL, W. WEBER, E. IPPISCH, U. HAGELAUER, O. WESS, W. HEPP, W. BRENDEL and G. PAUMGARTNER, *Shock-Wave Lithotripsy of Gallbladder Stones*, New England Journal of Medicine, 318 (1988), pp. 393-397.
- [6] C. C. CHURCH, *A theoretical study of cavitation generated by an extracorporeal shock wave lithotripter*, The Journal of the Acoustical Society of America, 86 (1989), pp. 215-227.
- [7] R. P. FEDKIW, T. ASLAM, B. MERRIMAN and S. OSHER, *A Non-oscillatory Eulerian Approach to Interfaces in Multimaterial Flows (the Ghost Fluid Method)*, Journal of Computational Physics, 152 (1999), pp. 457-492.
- [8] X. HU and B. KHOO, *An Interface Interaction Method for Compressible Multi-Fluids*, Journal of Computational Physics, 198 (2004), pp. 35-64.
- [9] T. G. LIU, B. C. KHOO and K. S. YEO, *Ghost fluid method for strong shock impacting on material interface*, Journal of Computational Physics, 190 (2003), pp. 651-681.
- [10] S. SAMBASIVAN, *A sharp interface Cartesian grid hydrocode*, Theses and Dissertations (2010).
- [11] S. OSHER and J. A. SETHIAN, *Fronts propagating with curvature-dependent speed: Algorithms based on Hamilton-Jacobi formulations*, Journal of Computational Physics, 79 (1988), pp. 12-49.

- [12] G. RUSSO and P. SMEREKA, *A Remark on Computing Distance Functions*, Journal of Computational Physics, 163 (2000), pp. 51-67.
- [13] C. MIN and F. GIBOU, *A second order accurate level set method on non-graded adaptive cartesian grids*, Journal of Computational Physics, 225 (2007), pp. 300-321.
- [14] Z. SOLOMENKO, P. D. M. SPELT, L. Ó NÁRAIGH and P. ALIX, *Mass conservation and reduction of parasitic interfacial waves in level-set methods for the numerical simulation of two-phase flows: A comparative study*, International Journal of Multiphase Flow, 95 (2017), pp. 235-256.
- [15] X. Y. HU and B. C. KHOO, *An interface interaction method for compressible mult fluids*, Journal of Computational Physics, 198 (2004), pp. 35-64.
- [16] C. W. WANG, T. G. LIU and B. C. KHOO, *A Real Ghost Fluid Method for the Simulation of MultimediuM Compressible Flow*, SIAM Journal on Scientific Computing, 28 (2006), pp. 278-302.
- [17] S. K. SAMBASIVAN and H. S. UDAYKUMAR, *Ghost Fluid Method for Strong Shock Interactions Part 1: Fluid-Fluid Interfaces*, AIAA Journal, 47 (2009), pp. 2907-2922.
- [18] N. BEMPEDELIS and Y. VENTIKOS, *A simplified approach for simulations of multidimensional compressible multicomponent flows: The grid-aligned ghost fluid method*, Journal of Computational Physics, 405 (2020), pp. 109129.
- [19] S. K. SAMBASIVAN and H. S. UDAYKUMAR, *Sharp interface simulations with Local Mesh Refinement for multi-material dynamics in strongly shocked flows*, Computers & Fluids, 39 (2010), pp. 1456-1479.
- [20] P. DAS and H. S. UDAYKUMAR, *A sharp-interface method for the simulation of shock-induced vaporization of droplets*, Journal of Computational Physics, 405 (2020), pp. 109005.
- [21] J. LIN, H. DING, X. LU and P. WANG, *A Comparison Study of Numerical Methods for Compressible Two-Phase Flows*, Advances in Applied Mathematics and Mechanics, 9 (2017), pp. 1111-1132.
- [22] H. TERASHIMA and G. TRYGGVASON, *A front-tracking/ghost-fluid method for fluid interface in compressible flow*, Journal of Computational Physics, 228 (2009), pp. 4012-4037.
- [23] S. SHANKAR, S. KAWAI and S. LELE, *Numerical Simulation of Multicomponent Shock Accelerated Flows and Mixing using Localized Artificial*

*Diffusivity Method*, 48th AIAA Aerospace Sciences Meeting Including the New Horizons Forum and Aerospace Exposition (2010).

- [24] X. HU and B. KHOO, *Numerical studies on shock cell interaction*, Shock Waves, ISBN 978-3-540-22497-6. Springer-Verlag Berlin Heidelberg, 2005, p. 1205 (2005).
- [25] D. PENG, B. MERRIMAN, S. OSHER, H. ZHAO and M. KANG, *A PDE-Based Fast Local Level Set Method*, Journal of Computational Physics, 155 (1999), pp. 410-438.
- [26] M. SUSSMAN, P. SMEREKA and S. OSHER, *A Level Set Approach for Computing Solutions to Incompressible Two-Phase Flow*, Journal of Computational Physics, 114 (1994), pp. 146-159.
- [27] S. GOTTLIEB and C.-W. SHU, *Total Variation Diminishing Runge-Kutta Schemes*, Mathematics of Computation, 67 (1998), pp. 73-85.
- [28] G.-S. JIANG and C.-W. SHU, *Efficient Implementation of Weighted ENO Schemes*, Journal of Computational Physics, 126 (1996), pp. 202-228.
- [29] D. HARTMANN, M. MEINKE and W. SCHRÖDER, *The constrained reinitialization equation for level set methods*, Journal of Computational Physics, 229 (2010), pp. 1514-1535.
- [30] A. DU CHÉNÉ, C. MIN and F. GIBOU, *Second-Order Accurate Computation of Curvatures in a Level Set Framework Using Novel High-Order Reinitialization Schemes*, Journal of Scientific Computing, 35 (2008), pp. 114-131.
- [31] C.-W. SHU, *High Order Weighted Essentially Nonoscillatory Schemes for Convection Dominated Problems*, SIAM Review, 51 (2009), pp. 82-126.
- [32] P. L. ROE, *Approximate Riemann solvers, parameter vectors, and difference schemes*, Journal of Computational Physics, 43 (1981), pp. 357-372.
- [33] E. TORO, *Riemann Solvers and Numerical Methods for Fluid Dynamics: A Practical Introduction*, 2009.
- [34] S. OSHER, *Level set methods and dynamic implicit surfaces*, (2003).
- [35] D. HARTMANN, M. MEINKE and W. SCHRÖDER, *Differential equation based constrained reinitialization for level set methods*, Journal of Computational Physics, 227 (2008), pp. 6821-6845.

- [36] R. R. NOURGALIEV, N. DINH and T. THEOFANOUS, *Adaptive Characteristics -Based Matching for Compressible Multifluid Dynamics*, Journal of Computational Physics, 213 (2006), pp. 500-529.
- [37] X. Y. HU, B. C. KHOO, N. A. ADAMS and F. L. HUANG, *A conservative interface method for compressible flows*, Journal of Computational Physics, 219 (2006), pp. 553-578.
- [38] J. LUO, X. Y. HU and N. A. ADAMS, *A conservative sharp interface method for incompressible multiphase flows*, Journal of Computational Physics, 284 (2015), pp. 547-565.
- [39] J.-Y. LIN, Y. SHEN, H. DING, N.-S. LIU and X.-Y. LU, *Simulation of compressible two-phase flows with topology change of fluid–fluid interface by a robust cut-cell method*, Journal of Computational Physics, 328 (2017), pp. 140-159.
- [40] D. NGUYEN, F. GIBOU and R. FEDKIW, *A Fully Conservative Ghost Fluid Method Stiff Detonation Waves*, (2002).
- [41] M. J. BERGER and J. OLIGER, *Adaptive mesh refinement for hyperbolic partial differential equations*, Journal of Computational Physics, 53 (1984), pp. 484-512.
- [42] M. J. BERGER and P. COLELLA, *Local adaptive mesh refinement for shock hydrodynamics*, Journal of Computational Physics, 82 (1989), pp. 64-84.
- [43] P. MACNEICE, K. M. OLSON, C. MOBARRY, R. DE FAINCHEIN and C. PACKER, *PARAMESH: A parallel adaptive mesh refinement community toolkit*, Computer Physics Communications, 126 (2000), pp. 330-354.
- [44] C. SHEN, J.-M. QIU and A. CHRISTLIEB, *Adaptive mesh refinement based on high order finite difference WENO scheme for multi-scale simulations*, Journal of Computational Physics, 230 (2011), pp. 3780-3802.
- [45] D. DEZEEUW and K. G. POWELL, *An Adaptively Refined Cartesian Mesh Solver for the Euler Equations*, Journal of Computational Physics, 104 (1993), pp. 56-68.
- [46] K. M. OLSON and P. MACNEICE, *An Overview of the PARAMESH AMR Software Package and Some of Its Applications*, in T. Plewa, T. Linde and V. Gregory Weirs, eds., *Adaptive Mesh Refinement - Theory and Applications*, Springer Berlin Heidelberg, Berlin, Heidelberg, 2005, pp. 315-330.
- [47] K. OLSON, - *PARAMESH: A Parallel, Adaptive Grid Tool*, in A. Deane, A. Ecer, J. McDonough, N. Satofuka, G. Brenner, D. R. Emerson, J. Periaux and D.

Tromeur-Dervout, eds., *Parallel Computational Fluid Dynamics 2005*, Elsevier, Amsterdam, 2006, pp. 341-348.

- [48] G. M. MORTON, *A computer oriented geodetic data base and a new technique in file sequencing*, IBM Ltd. (1966).
- [49] R. LÖHNER, *An adaptive finite element scheme for transient problems in CFD*, *Computer Methods in Applied Mechanics and Engineering*, 61 (1987), pp. 323-338.
- [50] R. ABGRALL and S. KARNI, *Computations of Compressible Multifluids*, *Journal of Computational Physics*, 169 (2001), pp. 594-623.
- [51] S. KAWAI and H. TERASHIMA, *A high-resolution scheme for compressible multicomponent flows with shock waves*, *International Journal for Numerical Methods in Fluids*, 66 (2011), pp. 1207-1225.
- [52] M. CAPUANO, C. BOGEY and P. SPELT, *Simulations of viscous and compressible gas-gas flows using high-order finite difference schemes*, *Journal of Computational Physics*, 361 (2018), pp. 56-81.
- [53] R. SAUREL and R. ABGRALL, *A Simple Method for Compressible Multifluid Flows*, *Siam Journal on Scientific Computing*, 21 (1999), pp. 1115-1145.
- [54] J. F. HAAS and B. STURTEVANT, *Interaction of weak shock waves with cylindrical and spherical gas inhomogeneities*, *Journal of Fluid Mechanics*, 181 (1987), pp. 41-76.
- [55] J. J. QUIRK and S. KARNI, *On the dynamics of a shock-bubble interaction*, *Journal of Fluid Mechanics*, 318 (1996), pp. 129-163.
- [56] A. MARQUINA and P. MULET, *A flux-split algorithm applied to conservative models for multicomponent compressible flows*, *Journal of Computational Physics*, 185 (2003), pp. 120-138.
- [57] V. CORALIC and T. COLONIUS, *Finite-volume WENO scheme for viscous compressible multicomponent flows*, *Journal of Computational Physics*, 274 (2014), pp. 95-121.
- [58] M. BROUILLETTE, *THE RICHTMYER-MESHKOV INSTABILITY*, *Annual Review of Fluid Mechanics*, 34 (2002), pp. 445-468.
- [59] J. W. MILES, *On the generation of surface waves by shear flows Part 3. Kelvin-Helmholtz instability*, *Journal of Fluid Mechanics*, 6 (1959), pp. 583-598.

- [60] A. KUNDU and S. DE, *High resolution numerical simulation of a shock-accelerated refrigerant-22 bubble*, *Computers & Fluids*, 193 (2019), pp. 104289.
- [61] E. JOHNSEN and T. I. M. COLONIUS, *Numerical simulations of non-spherical bubble collapse*, *Journal of Fluid Mechanics*, 629 (2009), pp. 231-262.
- [62] R. K. SHUKLA, *Nonlinear preconditioning for efficient and accurate interface capturing in simulation of multicomponent compressible flows*, *Journal of Computational Physics*, 276 (2014), pp. 508-540.
- [63] N. A. HAWKER and Y. VENTIKOS, *Interaction of a strong shockwave with a gas bubble in a liquid medium: a numerical study*, *Journal of Fluid Mechanics*, 701 (2012), pp. 59-97.
- [64] L. N. HOWARD, *Hydrodynamic and Hydromagnetic Stability*. By S. CHANDRASEKHAR. Clarendon Press: Oxford University Press, 1961. 652 pp. £5. 5s, *Journal of Fluid Mechanics*, 13 (1962), pp. 158-160.
- [65] G. DIMONTE and P. RAMAPRABHU, *Simulations and model of the nonlinear Richtmyer-Meshkov instability*, *Physics of Fluids - PHYS FLUIDS*, 22 (2010).
- [66] M. LATINI, O. SCHILLING and W. S. DON, *Effects of WENO flux reconstruction order and spatial resolution on reshocked two-dimensional Richtmyer–Meshkov instability*, *Journal of Computational Physics*, 221 (2007), pp. 805-836.
- [67] T. D. ASLAM, *A partial differential equation approach to multidimensional extrapolation*, *Journal of Computational Physics*, 193 (2004), pp. 349-355.
- [68] Y. HAO and J. PENG, *Numerical study of the shear-thinning effect on the interaction between a normal shock wave and a cylindrical liquid column*, *Physics of Fluids*, 31 (2019).